





# Distinct pre-initiation steps in human mitochondrial translation

Anas Khawaja<sup>1,2,7</sup>, Yuzuru Itoh <sup>1,3,7</sup>, Cristina Remes<sup>4</sup>, Henrik Spåhr<sup>1,2,4</sup>, Olessya Yukhnovets<sup>5,6</sup>, Henning Höfig <sup>5,6</sup>, Alexey Amunts <sup>1,3</sup>✉ & Joanna Rorbach <sup>1,2</sup>✉

Translation initiation in human mitochondria relies upon specialized mitoribosomes and initiation factors, mtIF2 and mtIF3, which have diverged from their bacterial counterparts. Here we report two distinct mitochondrial pre-initiation assembly steps involving those factors. Single-particle cryo-EM revealed that in the first step, interactions between mitochondria-specific protein mS37 and mtIF3 keep the small mitoribosomal subunit in a conformation favorable for a subsequent accommodation of mtIF2 in the second step. Combination with fluorescence cross-correlation spectroscopy analyses suggests that mtIF3 promotes complex assembly without mRNA or initiator tRNA binding, where exclusion is achieved by the N-terminal and C-terminal domains of mtIF3. Finally, the association of large mitoribosomal subunit is required for initiator tRNA and leaderless mRNA recruitment to form a stable initiation complex. These data reveal fundamental aspects of mammalian protein synthesis that are specific to mitochondria.

<sup>1</sup> Department of Medical Biochemistry and Biophysics, Division of Molecular Metabolism, Karolinska Institutet, Biomedicum, 171 65 Solna, Sweden. <sup>2</sup> Max Planck Institute Biology of Ageing - Karolinska Institutet Laboratory, Karolinska Institutet, Stockholm, Sweden. <sup>3</sup> Science for Life Laboratory, Department of Biochemistry and Biophysics, Stockholm University, 17165 Solna, Sweden. <sup>4</sup> Department of Mitochondrial Biology, Max-Planck-Institute for Biology of Ageing, Joseph-Stelzmann-Str. 9b, 50931 Cologne, Germany. <sup>5</sup> RWTH Aachen, I. Physikalisches Institut (IA), Aachen, Germany. <sup>6</sup> Forschungszentrum Jülich, Institute of Complex Systems ICS-5, Jülich, Germany. <sup>7</sup> These authors contributed equally: Anas Khawaja, Yuzuru Itoh. ✉email: [amunts@scilifelab.se](mailto:amunts@scilifelab.se); [joanna.rorbach@ki.se](mailto:joanna.rorbach@ki.se)

The genome of human mitochondria encodes for thirteen proteins that require specialized mitoribosomes for their synthesis. The specialization of the mitoribosomes is illustrated by the reduction of rRNA and addition of specific proteins, for many of which the functions are not known<sup>1,2</sup>. The process of protein synthesis starts with translation initiation. The canonical bacterial translation begins with the initiation factors IF1, IF2, IF3, and initiator tRNA that assemble on the small ribosomal subunit (SSU) to recognize the mRNA start codon, followed by the joining of the large subunit (LSU). The Shine–Dalgarno (SD) sequence is used to recruit mRNA to SSU through the anti-SD of the rRNA. However, in human mitochondria the mRNAs and the mitoribosome do not have the respective SD and anti-SD sequences. In addition, IF1 is missing compared to the bacterial system, whereas the GTPase mtIF2 and mtIF3 have specific extensions. Mitochondrial mRNAs are also different as most of them do not possess 5' leader sequences, further highlighting special requirements for translation initiation.

A complete mitochondrial translation initiation complex with the joint mitoribosomal subunits has been reconstituted from bovine components<sup>3</sup>, and mtIF3 has been identified as a crucial component for initiation in mouse<sup>4</sup>. However, how the initiation complex is formed and which structural elements of the mitoribosome, initiation factors, and the interplay between them lead to the full assembly is not known. To investigate how translation initiation starts in human mitochondria, we analyze here the early involved complexes of the small mitoribosomal subunit using a combination of cryo-EM, fluorescence cross-correlation spectroscopy, and single-molecule fluorescence techniques. Our data reveal two defined steps that lead to the mitochondrial translation initiation, termed mitochondrial preinitiation steps 1 and 2 (mtPIC-1, mtPIC-2), which explains how mitochondria-specific extensions of initiation factors interact with mitoribosomal proteins to govern the mechanism of translation.

## Results

**Structure determination of mitochondrial preinitiation translation complexes.** We first purified the mtIF3-bound mitoribosomal SSU (mtSSU) by immunoprecipitation from HEK293 cells overexpressing 3xFLAG-tagged mtIF3. In bacteria, the preinitiation complex can be formed by adding IF2 to the SSU-IF3 complex in the presence of a nonhydrolyzable GTP analogue (GDPNP), formylmethionyl-tRNA<sup>Met</sup><sub>i</sub> (fMet-tRNA<sup>Met</sup><sub>i</sub>), and mRNA<sup>5</sup>. Therefore, we incubated the pulled-down mtSSU-mtIF3 with purified recombinant human mtIF2 in the presence of GDPNP, *Escherichia coli* fMet-tRNA<sup>Met</sup><sub>i</sub>, and leaderless mRNA (MT-CO2). To determine the structure of the complex, a cryo-EM density map was calculated from a subset of 552,920 particles and signal subtraction was applied using a mask for the entire complex except the mtIF3-binding site, followed by 3D classification using the mask for the mtIF3-binding site (Supplementary Fig. 1). Subsequently, particles containing mtIF3 were further classified with signal subtraction on mtIF2, which resulted in two maps at 3.0 Å and 3.1 Å resolution, containing mtIF3 and mtIF2-mtIF3, respectively (Supplementary Figs. 2–5, Supplementary Tables 1, 2). No fMet-tRNA<sup>Met</sup><sub>i</sub> or mRNA was detected on the mtSSU, suggesting that the identified arrangements are the most stable and likely represent states prior to the binding of tRNA and mRNA, namely mitochondrial preinitiation (mtPIC) (Fig. 1).

### The conformational rigidity of mtIF3 preserves vacant mtPIC.

In bacteria, the conventional description of the translation preinitiation pathway implies large-scale changes in IF3 that define its distinct role during the process, including accommodation of

the fMet-tRNA<sup>Met</sup><sub>i</sub> into the P site for start codon recognition<sup>5</sup>. In mitochondria, mtIF3 adopts a more extended topology that includes N- and C-terminal domains (NTD, CTD) flanked by mitochondria-specific extensions (NTE, CTE) and joined by a helical linker (Fig. 2). In our mtSSU-mtIF3 (mtPIC-1) structure, the CTD is bound to h24 (1077–1080) and h44 (1480, 1560–1562), where the rRNA sequence differs from bacteria (Fig. 2, Supplementary Table 3). This mode of binding overlaps with two conserved inter-subunit rRNA bridges B2a and B2b, blocking the premature association of the mitoribosomal LSU (mtLSU). In addition, the helical linker would interfere with H68 of the mtLSU. The NTD residues of mtIF3 (S76, N77, D113, and R115) also form interactions with h23 and uS11m (T114, R118, and R138) close to uS7m and mS37 (Fig. 2a, Supplementary Table 3), while in bacteria no substantial interactions with IF3-NTD have been reported<sup>5</sup> (Supplementary Fig. 6a). The NTD residues of mtIF3 that interact with the mtSSU are highly conserved amongst vertebrates, but not in bacteria (Supplementary Fig. 6c).

The position of CTD also overlaps with the fMet-tRNA<sup>Met</sup><sub>i</sub> binding site on mtSSU, which is similar in bacteria where IF3-CTD needs to be relocated on SSU to accommodate fMet-tRNA<sup>Met</sup><sub>i</sub><sup>5</sup>. Prior to this, bacterial IF3-NTD moves away from the platform to about 36 Å from its original position, to bind the elbow of fMet-tRNA<sup>Met</sup><sub>i</sub>. This relocation is unlikely in mitochondria, due to the multiple contacts between mtIF3 and mtSSU. Moreover, while in bacteria the surface of the NTD of IF3 that interacts with fMet-tRNA<sup>Met</sup><sub>i</sub> is positively charged, allowing RNA-protein interaction, mtIF3-NTD has a negative electrostatic potential (Supplementary Fig. 6b) and the residues that interact with the tRNA elbow in bacteria are not conserved in mtIF3 (Supplementary Fig. 6c). This implies that mtIF3-NTD cannot interact efficiently with tRNA. Importantly, the residues responsible for tRNA discrimination in bacteria<sup>6,7</sup> are not conserved in mtIF3 (Supplementary Fig. 6c).

These data suggest an extensive network of contacts between mtIF3 and mtSSU that synergistically stabilize the association. Such mode of binding provides structural constraints that limit the range of conformational flexibility of mtIF3 on the mitoribosome in the preinitiation state, preventing it from sampling different positions. Therefore, mtIF3 appears to be more rigid on the mitoribosome, which is in contrast to bacterial species, where IF3 flexibility is essential for tRNA binding along the translation preinitiation pathway.

The observed conformation of the mitochondria-specific CTE of mtIF3 can also contribute to preserving vacant mtPIC. The CTE is an  $\alpha$ -helix facing away from the mtSSU (Supplementary Fig. 7a) and its orientation is stabilized by specific interactions with the CTD (Fig. 2b). The CTE occupies the binding site of the acceptor stem of the fMet-tRNA<sup>Met</sup><sub>i</sub>, illustrated by superimposition with the complete initiation complex containing fMet-tRNA<sup>Met</sup><sub>i</sub>, which shows mutual exclusivity with mtIF3 (Supplementary Fig. 7b). Therefore, mtIF3 has to leave to allow the complete initiation complex to fully assemble. The comparison of the mtSSU-mtIF3 interactions with the recently reconstituted complex of bovine mtSSU and human mtIF3<sup>8</sup> shows that most of them have not been identified before (detailed analysis is given in Supplementary Fig. 8 and Supplementary Table 3).

To further investigate the formation of the translation initiation complex, we used in vitro fluorescence cross-correlation spectroscopy with fMet-tRNA<sup>Met</sup><sub>i</sub>, mtIF3, and MT-CO2 mRNA labeled with spectrally distinct fluorophores, in the presence of unlabeled mtIF2. The analysis showed that mtIF3 and fMet-tRNA<sup>Met</sup><sub>i</sub> are not found on the same mtSSU particles (Fig. 3a, Supplementary Fig. 9). The functionality of

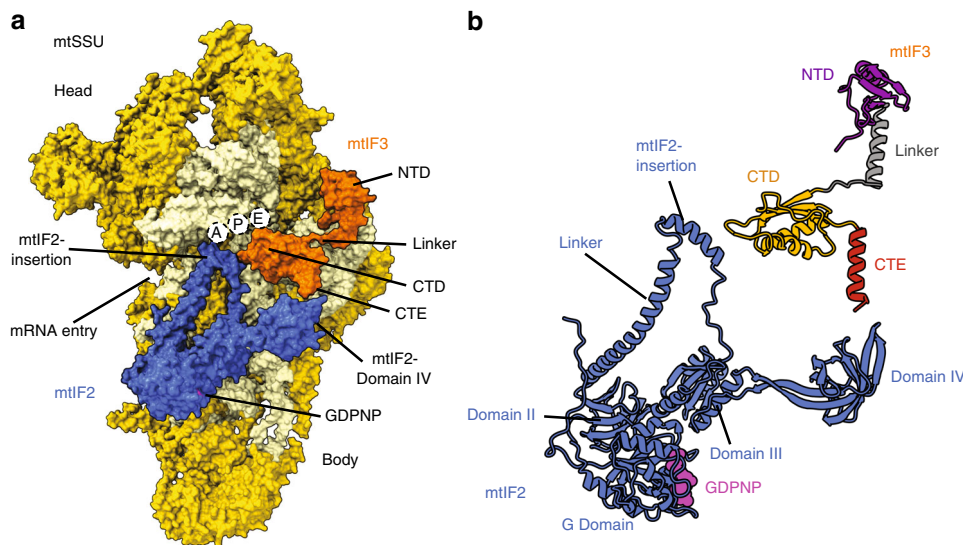


**Fig. 1 Structure of the human mitochondrial preinitiation translation complex (mtPIC-2).** **a** Surface representation of the mtSSU with mtIF3 (orange) and mtIF2 (blue). Empty tRNA-binding sites and mRNA channel are indicated. The binding of mtIF2 is accomplished due to mtIF3 NTD restricting the mtSSU head movement. **b** Relative positions of mtIF3 colored by domains (NTD purple, linker dark gray, CTD orange, CTE red) and mtIF2.

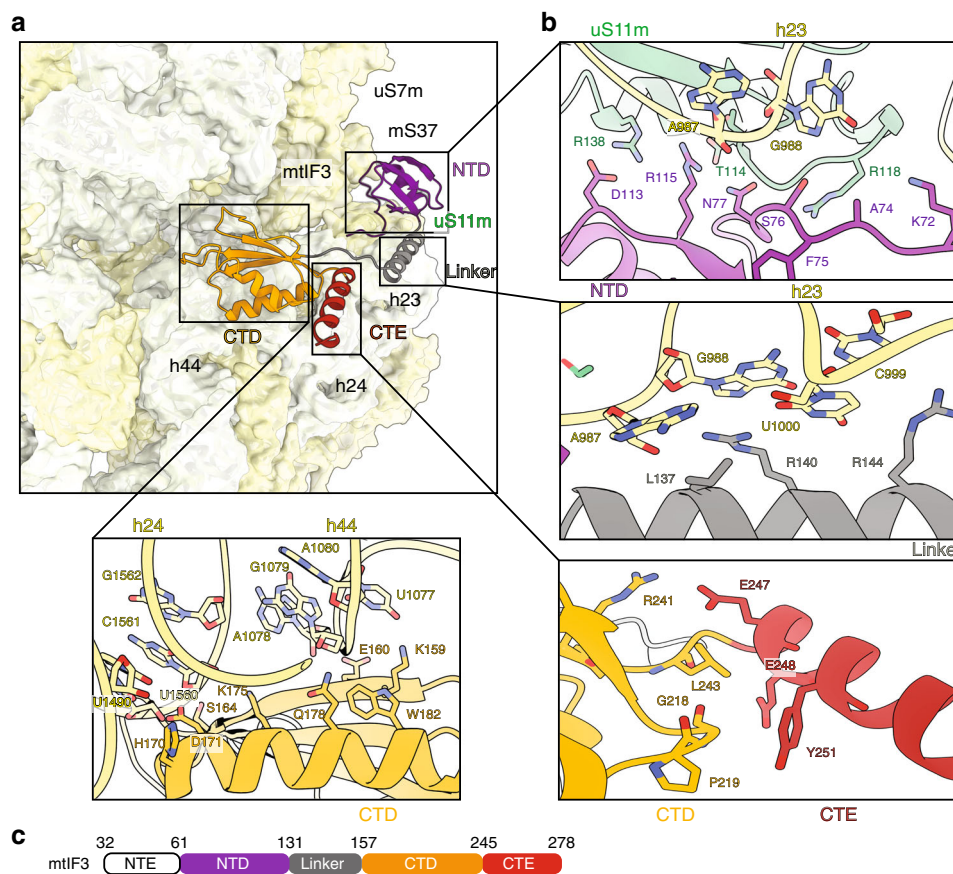


**Fig. 2 Multiple interactions of mtIF3 with the mtSSU.** **a** Domain organization of mtIF3 on mtSSU with mitochondria-specific CTE (red) positioned outward from mtSSU. **b** Zoom-in panels for each of the mtIF3 domains featuring interactions with mtSSU. **c** Schematic representation of the mtIF3 with the corresponding color-code. NTE is disordered in the structure.

the mtPIC was then analyzed by its ability to form a complete initiation complex when mixed with the mtLSU in the presence of mtIF2 (GTP), Cy3-labeled fMet-tRNA<sup>Met</sup><sub>i</sub> and mt-mRNA labeled at the 3' end with an Atto390 fluorophore (Fig. 3b). Correct formation of the complete initiation complex was

confirmed by fluorescence emission of both the Atto390 and Cy3 fluorophores, revealing that both the mRNA and fMet-tRNA<sup>Met</sup><sub>i</sub> are bound. Notably, no binding of mt-mRNA to the mtSSU was observed in our experimental conditions (Supplementary Table 4).

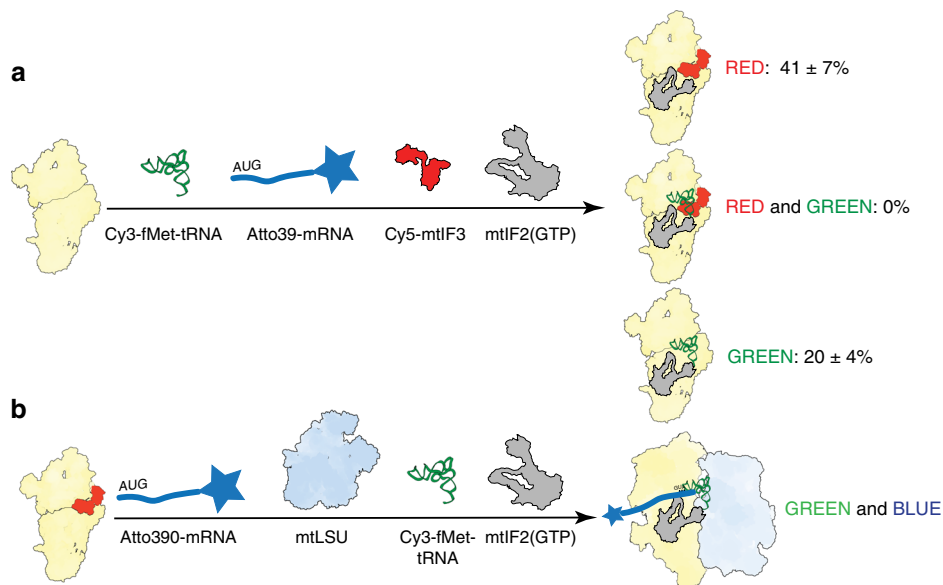


**Fig. 3** Binding of mtIF3 and fMet-tRNA<sup>fMet</sup> to the mtSSU is mutually exclusive. **a** Two-color fluorescence cross-correlation spectroscopy analysis of the initiation complex components. The mtSSU was incubated with an excess of Cy3-fMet-tRNA<sup>fMet</sup>, Cy5-mtIF3, mtIF2(GTP), and Atto390-mRNA, then purified by a sucrose gradient. Products may contain unlabeled mtIF2. **b** The functionality of mtPIC was validated by the ability to form a complete initiation complex when incubated with an excess of mtLSU, Cy3-fMet-tRNA<sup>fMet</sup>, Atto390-mRNA, and unlabeled mtIF2 (GTP). After purification of the monosome, detection of both Cy3 and Atto390 fluorophores confirmed binding of mRNA and tRNA. Source data are provided as a Source Data file.

**Mitoribosomal protein mS37 restricts the head swiveling for the accommodation of mtIF2.** In bacteria, binding of IF3, IF1, and mRNA to the SSU stabilizes a swiveled conformation of the SSU head with respect to the body that consequently allows IF2 to bind and advance to the next step in the initiation process<sup>5,9</sup>. However, mitochondria lack IF1, and as our structure shows, no mRNA is detected in mtPIC-1. Therefore, to reveal the mechanism for stabilization of the mtSSU head in mtPIC-1, we performed a computational analysis of the head movement.

In the first step, the 3D classification showed similar but distinct head positions, indicating a continuous movement. To better distinguish between the states and rationalize the motion, we subsequently performed 3D multibody with a principal component analysis of the relative orientations of the head and body for all the particle images<sup>10</sup> (Fig. 4). The relative orientations are mainly described by three eigenvectors and only the vector that corresponds to the head swiveling shows a non-Gaussian distribution, suggesting that this motion is the most prominent in mtPIC-1 (Fig. 4d–f). Comparison between maps based on head swiveling establishes a correlation between the position of mS37 and the presence of mtIF3-NTD. In particular, when mS37 is in its closest proximity to the mtIF3-binding site (closed state), the density for mtIF3-NTD is weaker (Fig. 4g–h), suggesting their incompatibility.

The mS37 is a mitochondria-specific 13.5 kDa protein, with a coiled-coil-helix domain<sup>11</sup>, peripherally bound at the mRNA channel exit<sup>1</sup>. Its motion around the mtSSU vertical axis is driven by the rotation of the internal rRNA h28, which forms the neck. The h28 is most compressed in the closed state, as can be seen through the movement of equivalent atoms in different states (Supplementary Fig. 10). A careful inspection of the density in this region reveals an alternative conformation of the h28-associated region of uS7m ( $\beta$ -hairpin motif I156-P173 and the C-terminus N233-W282) that represents an even more compressed conformation of h28 (Supplementary Fig. 10). Since a more closed head conformation would result in a clash with the mtIF3, it suggests that the functional role of mS37 is to restrict the degrees of freedom of the mtSSU head swiveling in mtPIC-1.

Taken together, our structural information suggests that the interplay between mS37 and mtIF3 is the mechanism that keeps the mtSSU head a favorable position for the consequent accommodation of mtIF2 (Supplementary Fig. 11).

### The conformational rearrangement of mtIF2 is required for translation initiation progress.

The factor mtIF2 is a multi-domain GTPase that comprises four conserved domains and a mitochondria-specific insertion of 37 amino acids between its helical and linker regions (Fig. 5). In our mtSSU-mtIF2-mtIF3 (mtPIC-2) structure, mtIF2 adopts a similar conformation to its bacterial counterpart<sup>5,12</sup>, but with some important differences. The  $\alpha$ -helical mtIF2 insertion spans the same binding pocket as bacterial IF1, blocking the A-site, as previously suggested<sup>13,14</sup> (Fig. 1). The insert establishes contacts mostly through hydrogen bonding with h18 (889–892) and uS12m (Fig. 5, Supplementary Table 5). The linker comprising the loop region (K504-R509) connected to domain III interacts with h44 (1493–1496) and uS12m (Fig. 5b, Supplementary Table 5). These specific interactions of mtIF2 with mtSSU can affect the conformational space of the mtSSU head, which is different from mtPIC-1 and bacterial counterparts, as revealed by the 3D multibody analysis (Supplementary Fig. 12). Thus, the data suggest that the role of mtIF2 in mtPIC-2 is to stabilize the assembly and prepare it for the following step.

During the next step of the initiation pathway, the mtLSU is accommodated. To understand the structural rearrangements required for this event to occur, we compared the structures of mtPIC-2 and the complete initiation monosome complex<sup>3</sup>. Our analyses revealed three major features: (i) the mtIF2 globular domain IV undergoes a profound conformational change, reflected in 22 Å movement for R613, whereas the C-terminus remains anchored (Fig. 5a); (ii) h44 is rearranged, losing interaction with the mtIF2 linker (Supplementary Fig. 13 and 14, Supplementary Table 5); (iii) the G-domain of mtIF2 is found in two different GTPase states, namely preactive in mtPIC-2 and active in the complete initiation complex. The G-domain-bound GDPNP is

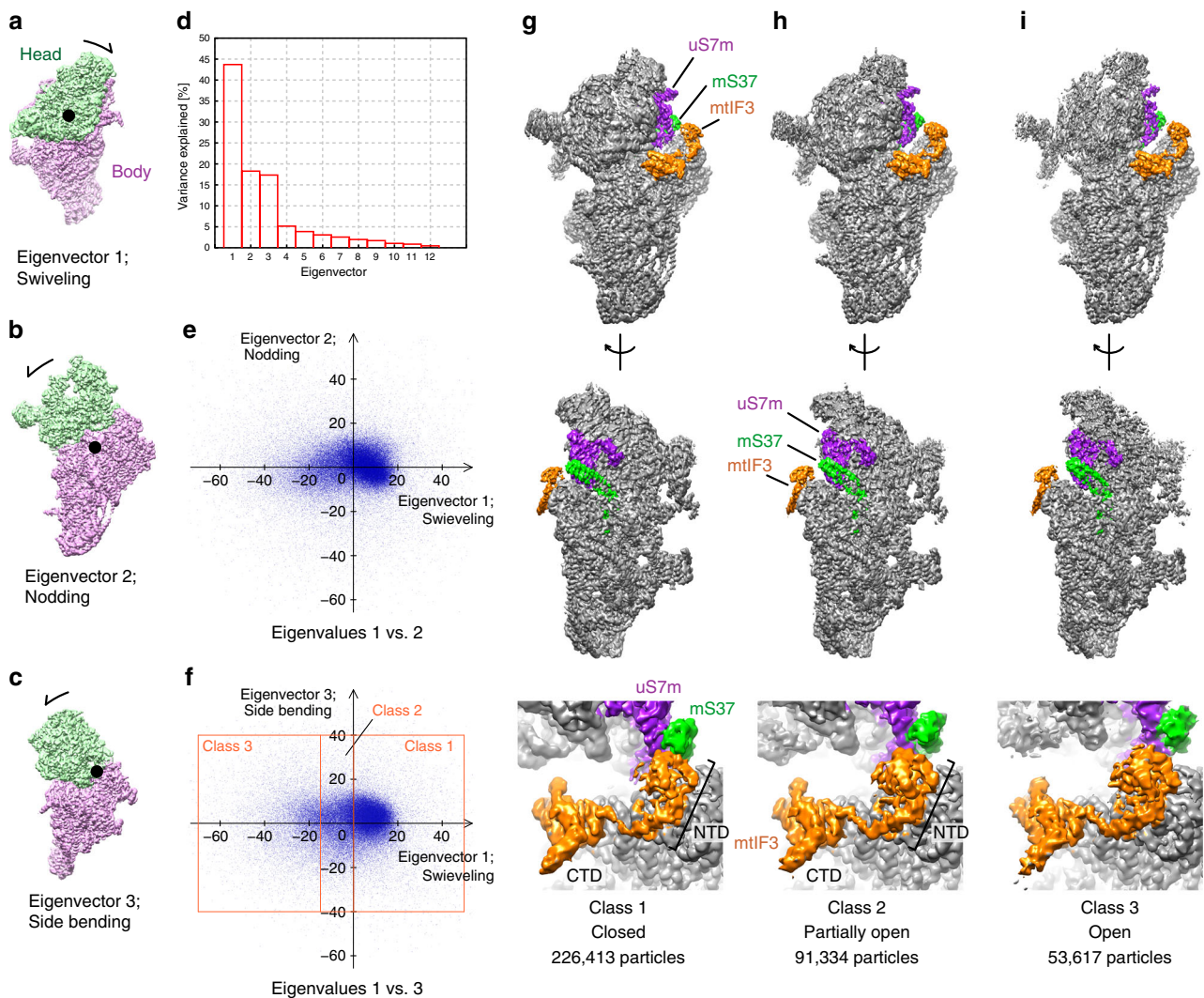


**Fig. 4 Principal component analysis of the mtSSU head motion suggests a function for the mitoribosomal protein mS37 in restricting the swiveling.** a–c

The relative orientation of the head to the body is described by 12 eigenvectors, representing translation and rotation in each particle. The eigenvectors 1, 2, and 3 were found to mainly contribute to the head motion, as indicated. **d** Histogram of the variances explained by the 12 eigenvectors. **e, f** The 1st to 3rd eigenvalues of randomly chosen particles represented by dots are plotted against each other, showing non-gaussian distribution for the swiveling motion. The particles are classified based on the values of eigenvector 1 (rectangles). **g, h** Comparison between the reconstructions of the classified particles. The closed conformation (Class 1) exhibits weaker density for the mtIF3-NTD interacting with mS37 and uS7m, compared to the other conformations with higher particle numbers.

found in close proximity to the mtIF2-domain III and the C-terminus, and the transition between mtPIC-2 and the complete initiation complex involves a switch of the catalytic and conserved H238 (Supplementary Fig. 15). Particularly, in mtPIC-2, H238 is rotated away from the  $\gamma$ -phosphate of GDPNP, representing the preactive conformation, whereas in the complete complex it primarily adopts an inward facing conformation activating GTP hydrolysis. Moreover, the region encompassing the P-loop and switch I display subtle rearrangements, particularly V189 and I213, which form the hydrophobic gate and appear important for the GTPase activity (Supplementary Fig. 15). The dynamics of mtIF2-domain IV between the two initiation stages causes a subtle reordering of its C-terminus, notably of F727, which lies adjacent to the catalytic H238 (Supplementary Fig. 15). The correlation between the mtLSU incorporation, the conformational change of h44 and mtIF2, and GTPase activation suggests that the flexibility of domain IV reported here is crucial for the formation of the complete initiation complex.

**Leaderless mt-mtRNA forms a stable complex with the monosome during translation initiation.** In bacteria, binding of the canonical mRNA to the SSU, which involves base pairing between a SD and anti-SD sequence upstream of the start codon, is a prerequisite for subunits joining and formation of the complete initiation complex. Notably, neither in our structural studies nor fluorescence analysis was leaderless mt-mRNA detected on the mtSSU. Instead, mt-mRNA was only found in the complete initiation complex (Fig. 3b). To further investigate the binding of leaderless mRNA to the mitoribosome, initiation reactions were made by incubating MT-CO2 mRNA hybridized to biotinylated lambda DNA (Fig. 6a) with either double-labeled monosome (labeled with Cy5 at the mtSSU and with Atto488 at the mtLSU) or Cy5-labeled mtSSU (Fig. 6b). Binding of the mitoribosomal subunits to mRNA was examined by simultaneous dual-color imaging using C-Trap™ optical tweezers combined with confocal microscopy. In these experimental conditions, we observed binding of the leaderless mRNA construct (but not mRNA

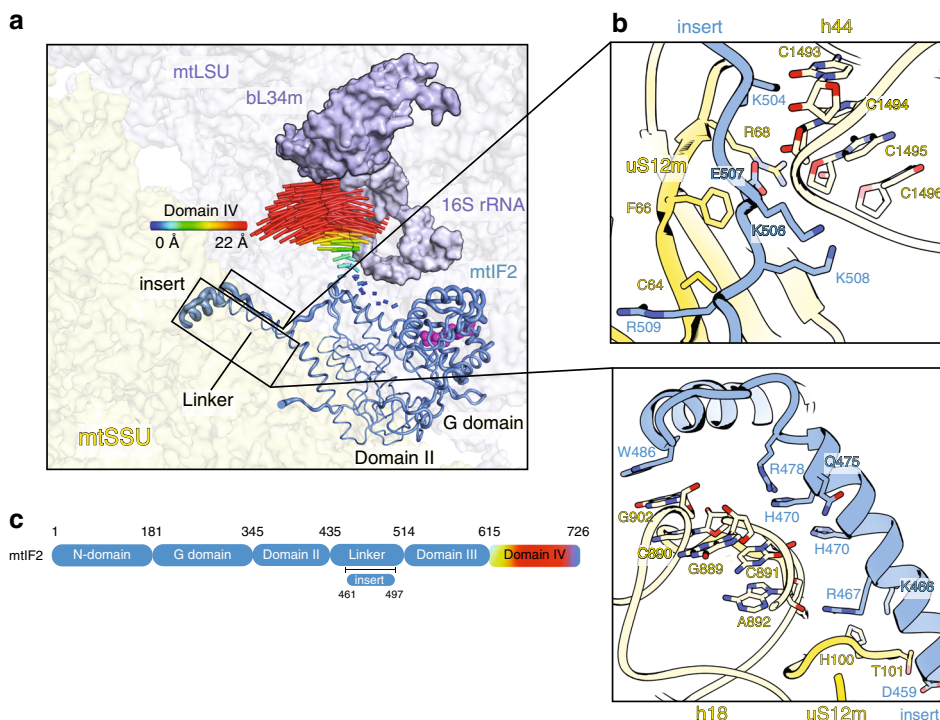


**Fig. 5** Contacts between mtIF2 and mtSSU in mtPIC-2, and conformational changes upon mtLSU association. **a** Comparison of mtIF2 binding in mtPIC-2 with the complete initiation complex (PDB ID: 6GAW). Upon association of the mtLSU (blue), required for complete initiation complex, the mtIF2-domain IV moves towards the mtSSU. The conformational change is represented by the difference vectors for each C $\alpha$  atom of domain IV. For the other domains, the flexibility is represented through ribbon thickness according to B-factor. **b** Zoom-in panels showing contacts of the mtIF2-specific insert and linker domain with the mtSSU. **c** Schematic representation of the mtIF2 with the corresponding color-code to the conformational changes.

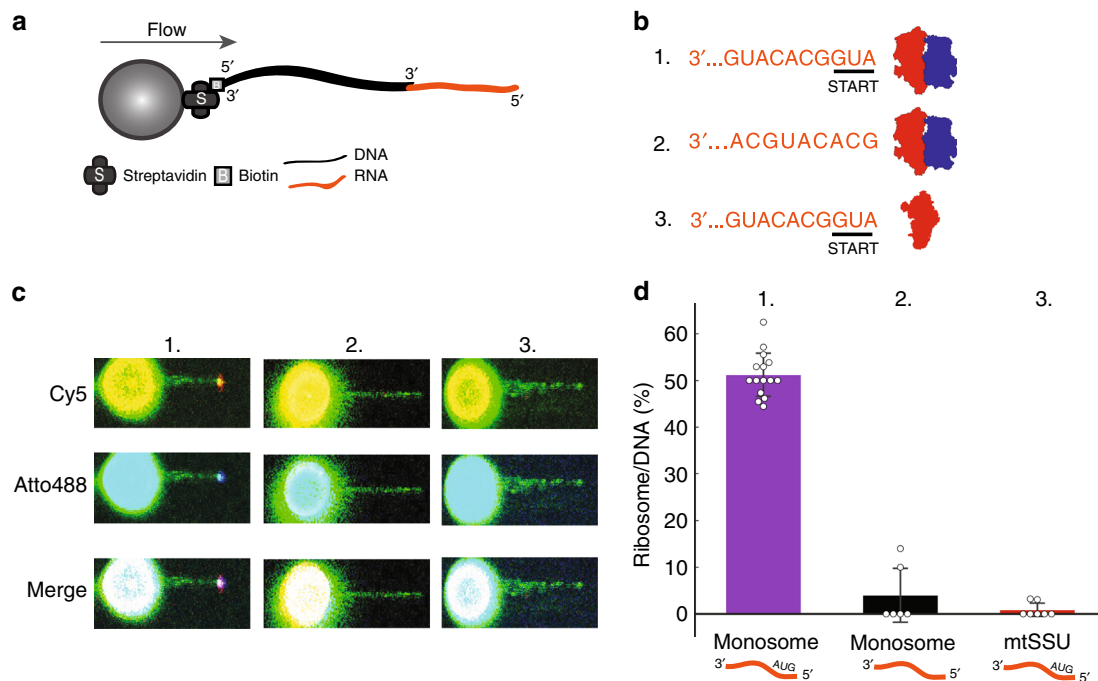


**Fig. 6** Binding of leaderless mt-mRNA to the monosome. **a** An optical tweezers setup to study mitochondrial translation initiation. RNA construct containing the first 51 nucleotides of MT-CO2 mRNA was ligated to biotinylated lambda DNA, allowing the 5'-end accessible for mitoribosome binding. **b** In order to monitor both mitoribosomal subunits, mtLSU and mtSSU were labeled with Cy5 and Atto488, respectively, and initiation reactions were made by incubating either double-labeled monosome (b, 1.) or Cy5-labeled mtSSU (b, 3.) with the DNA/RNA hybrid, mtIF3, mtIF2 (GTP), and fMet-tRNA<sup>Met</sup>. An RNA construct without start codon was used as a negative control (b, 2.). **c** Representative images showing binding of the mitoribosomal subunits tested by simultaneous dual-color confocal imaging. **d** Quantification of the binding events. The number of detected fluorescently labeled species were normalized to the number of trapped imaged DNA. Bars represent mean  $\pm$  SD. Source data are provided as a Source Data file.

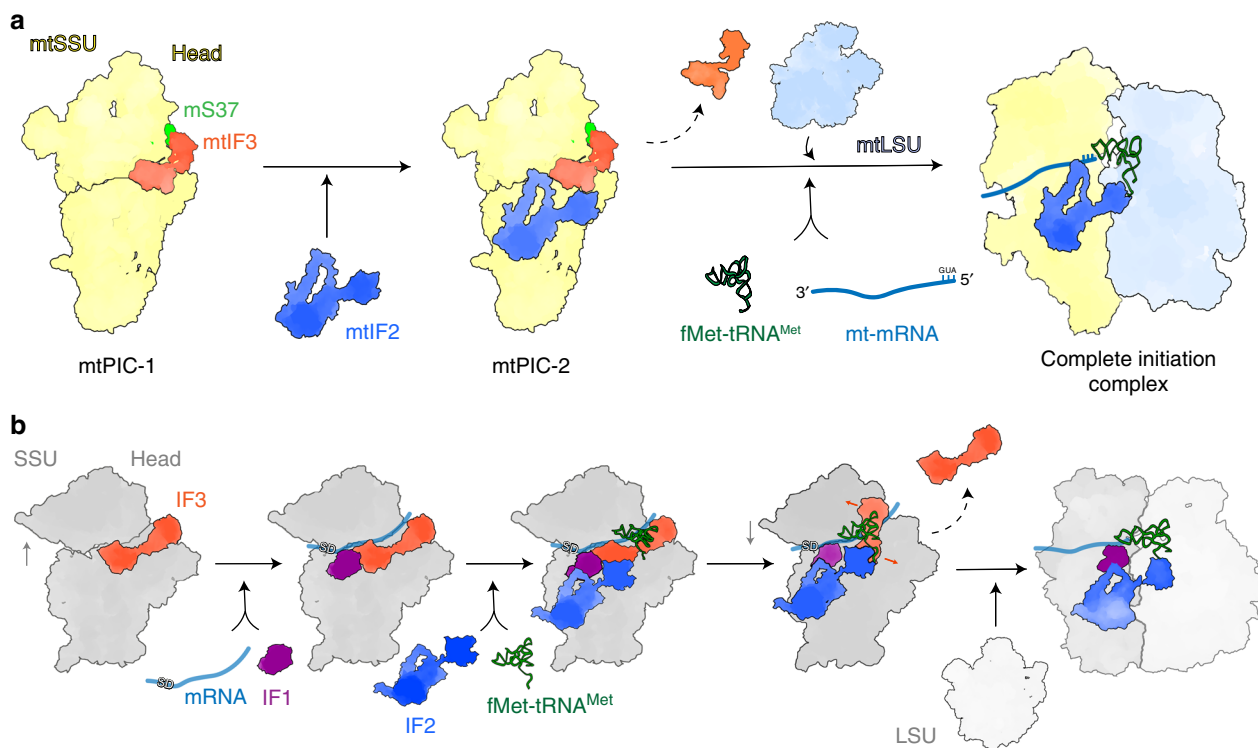


**Fig. 7 Model of mitochondrial translation initiation and comparison with the bacterial system. a** Translation initiation in mammalian mitochondria. The various structures are summarized in the order that represents a possible initiation pathway in which mtIF2 binding precedes mtLSU and tRNA binding. In this pathway, mtIF3 and mS37 stabilize the mtSSU head for the accommodation of mtIF2. Joining of the mtLSU may result in the conformational change of mtIF2 and GTPase activation that leads to tRNA and mRNA accommodation. Alternatively, transient binding of both mRNA and tRNA (not detected with our techniques) to the mtSSU after mtIF3 departure precede recruitment of the mtLSU. **b** Translation initiation in bacteria. Binding of canonical mRNA, fMet-tRNA<sup>Met</sup>, and initiator factors precede subunit joining and formation of the complete initiation complex.

without a start codon) to the monosome. As observed by cryo-EM, no stable binding to the mtSSU was detected (Fig. 6c, d). This result is in-line with several studies showing that also bacterial leaderless mRNAs have a much higher affinity for monosome than SSU<sup>15,16</sup>.

## Discussion

In the present study, we applied cryo-EM and fluorescent analysis to reveal mitochondria-specific states leading to translation initiation in human cells. The data provide insights in to the role of the mitoribosomal-specific protein mS37 in stabilizing the mtSSU head in the presence of mtIF3, which is tightly bound to the mtSSU and prevents accommodation of the initiator tRNA. This state is defined as mtPIC-1. Subsequent accommodation of mtIF2 with preactivated GTPase results in the intermediate state, mtPIC2, that allows binding of the mtLSU, replacement of mtIF3 with initiator tRNA and accommodation of the mitochondrial leaderless mRNA, which leads to the formation of a complete elongation-competent initiation complex (Fig. 7).

Although we cannot explicitly state that the identified mtPIC-1 and mtPIC-2 are exclusive and rule out the possibility that other short-lived intermediate remained undetected, the stable association of mtIF2 and mtIF3 with the mtSSU, as well as mt-mRNA and mt-tRNA with the monosome, suggests that the visualized events are the most prevalent in the process of mitochondrial translation initiation (Fig. 7). Taken together, our results provide the snapshots of the non-canonical assembly of the translation initiation machinery in mitochondria that coevolved together with the distinct mt-mRNAs, mitoribosomal-specific proteins, and extensions of the initiation factors.

## Methods

**Generation of a mammalian cell line expressing mtIF3.** The FLP-In T-Rex human embryonic kidney 293T (HEK293T) cell line (Invitrogen), which allows for the generation of stable doxycycline-inducible expression of transgenes by FLP recombinase-mediated integration, was used to express the human mitochondrial IF3 (mtIF3). HEK293T cells were grown in DMEM containing 10% tetracycline-free FCS (Cloneteck) and supplemented with 100 µg/ml Zeocin (Invitrogen) and 15 µg/ml Blasticidin S (Invivogen, San Diego, CA). The pcDNA5/FRT/TO vector harbouring mtIF3 cDNA with its C-terminus carrying FLAG-tag preceded by an HRV 3 C cleavage sequence (PreScission Site): Leu-Glu-Val-Leu-Phi-Gln↓Gly-Pro and the pOG44 vector, harboring the FLP recombinase, were co-transfected with Lipofectamine3000 (Thermo Fisher), according to the manufacturer's instructions. Transfected cells were selected adding 15 µg/ml Blasticidin S and 100 µg/ml Hygromycin B to culture media. Approximately 2 to 3 weeks post transfection, positive colonies appeared and single colonies were picked and expanded. Protein expression was induced adding doxycycline (Sigma-Aldrich) to a final concentration of 50 ng/ml to culture media 48 h prior experimental analysis.

**Preparation of the mtPIC.** Cells overexpressing mtIF3 were collected, resuspended in an ice-cold hypotonic buffer (0.6 M mannitol, 100 mM Tris-HCl pH 7.5, 10 mM ethylenediaminetetraacetic acid (EDTA), 0.05% bovine serum albumin (BSA)) and ruptured using dounce-homogenizers. The intact mitochondria were isolated by differential centrifugation: the crude mitochondria were loaded on the sucrose gradient (1.0 M and 1.5 M sucrose, 20 mM Tris-HCl pH 7.5, 1 mM EDTA) and centrifuged for 1 h at 25,000 rpm. (SW41 Ti rotor, Beckman Coulter). The band formed by the mitochondria between 1 M and 1.5 M sucrose was collected and resuspended in 10 mM Tris-HCl pH 7.5 in 1:1 ratio. After centrifugation, the purified mitochondrial pellet was resuspended in mitochondrial freezing buffer (200 mM trehalose, 10 mM Tris-HCl pH 7.5, 10 mM KCl, 0.1% BSA, 1 mM EDTA), flash-frozen and stored at -80 °C.

The mitoribosome bound FLAG-tagged mtIF3 was purified by immunoprecipitation. The purified mitochondria were lysed by incubating at 4 °C for 20 min in the lysis buffer (25 mM HEPES-KOH pH 7.5, 5.0 mM Mg(OAc)<sub>2</sub>, 100 mM KCl, 2% (v/v) Triton X-100, 0.2 mM dithiothreitol (DTT), 1X cComplete EDTA-free protease inhibitor cocktail (Roche), 40 U/µl RNase inhibitor (Invitrogen). The lysate was centrifuged at 5000 × g for 5 min at 4 °C and the supernatant was added to ANTI-FLAG M2 Affinity Gel (Sigma-Aldrich),

equilibrated with the wash buffer (25 mM HEPES-KOH pH 7.5, 5.0 mM Mg(OAc)<sub>2</sub>, 100 mM KCl, 0.05% β-DDM). After 3 h incubation at 4 °C, the gel was washed with the wash buffer and mtIF3-bound complexes were eluted by additional incubation of 2 h with the PreScission protease (GE Healthcare) (2 U/μl). Prior to the addition, the original storage buffer of the protease was replaced by the wash buffer with 2.0 mM DTT by buffer exchange using the concentrator Vivaspin MWCO 30,000 PES (Sartorius).

**Preparation of mtIF2, mtIF3, MT-CO2 mRNA, *E. coli* fMet-tRNA<sup>Met</sup><sub>i</sub>.** A codon-optimized (Genscript) DNA construct corresponding to the mature form of human mtIF2 (amino acids 38–727) or human mtIF3 (amino acids 32–278) was cloned into a pET-24b vector (Novagen). Both constructs were expressed in Rosetta 2 cells (EMD chemicals) at 25 °C for 16 h in Magic Media (Thermo Fisher Scientific). After lysis, the proteins were purified over a His-Select Ni<sup>2+</sup> resin (Sigma–Aldrich) and dialyzed against H-0.2 (25 mM Tris-HCl pH 7.4, 0.5 mM EDTA, 10% glycerol, 1 mM DTT, 200 mM NaCl). Further purification was conducted over a HiLoad 16/60 Superdex 200 pg gel filtration column (GE Healthcare) in buffer H-0.2 lacking glycerol.

The first 30 or 51 nucleotides of mitochondrially encoded cytochrome C oxidase 2 (MT-CO2) mRNA was purchased from Sigma–Aldrich or Eurofins, respectively.

The unlabeled *E. coli* fMet-tRNA<sup>Met</sup><sub>i</sub> was generously provided by Prof. Marina Rodnina, and the fMet-tRNA<sup>Met</sup><sub>i</sub> labeled at the dihydrouridine residues with Cy3 by Prof. Barry S. Cooperman<sup>17</sup>.

**Reconstitution of the mtPIC.** The formation of the human mitochondrial mtPICs was achieved through initial purification of the mtSSU-bound mtIF3. The recombinant mtIF2 (1 μM) was preincubated with GDPNP (2.5 mM) to form mtIF2-GDPNP in the presence of buffer A (25 mM HEPES-KOH pH 7.5, 5.0 mM Mg(OAc)<sub>2</sub>, 100 mM KCl, 0.05% β-DDM) for 30 min at room temperature. The mtIF2-GDPNP mix was added to the mtIF3-bound mtSSU eluate (A<sub>260</sub> = 7.9) together with the fMet-tRNA<sup>Met</sup><sub>i</sub> (1 μM) and MT-CO2 mRNA (1 μM) and incubated for another 30 min at room temperature. Subsequently, samples were directly applied to prepare the cryo-EM grids.

**Cryo-EM and image processing.** Holy carbon grids (Quantifoil R2/2, 300 mesh) were covered with a thin carbon layer (~3 nm thickness) and glow-discharged with 20 mA for 30 s. The reconstituted sample (3 μl) was applied to the grids at 4 °C with 100% humidity. After 30 s incubation, the grids were blotted for 3.5 s and vitrified by plunge-freezing in liquid ethane using a Vitrobot<sup>™</sup> Mark IV (ThermoFisher). Images were collected on a Titan Krios electron microscope (ThermoFisher) operated at 300 kV and equipped with a K2 Summit direct electron detector (Gatan). Micrographs were obtained from automated data collections (EPU software, ThermoFisher) at ×165,000 magnification, yielding a pixel size of 0.83 Å. 4 s exposures yielded a total dose of ~30 e<sup>-</sup>/Å<sup>2</sup> in 20 frames, with defocus values ranging from -0.25 to -5.0 μm. A total of 13,831 micrographs were recorded and kept. Movie frames were aligned and averaged by global and local motion corrections by the program MotionCor2<sup>18</sup>. Contrast transfer function (CTF) parameters were estimated by Gctf<sup>19</sup>. Particles were picked by Gautomatch and 2D classified by RELION 3.0<sup>10</sup>. In the first round, particles were picked by Gaussian based picking, followed by reference-free 2D classification. Several representative 2D classes were used as references for the second-round picking. The picked particles were subjected to 2D classification to discard contaminants as well as mtLSU and monosome particles (Supplementary Fig. 1). The remaining particles underwent 3D refinement by RELION 3.0<sup>10</sup> using EMDB-2880<sup>3</sup> as a 3D reference, followed by 3D classification with local angular search to remove poorly aligned particles. Well-resolved classes were pooled and subjected to 3D refinement and CTF refinement by RELION 3.0.

For classifying on mtIF3, signal subtraction was performed by RELION 3.0 using a mask covering the entire complex except for mtIF3-binding site, followed by 3D classification without alignment using the mask covering only mtIF3-binding site. The particles with mtIF3 were further classified on mtIF2 by the same procedure as that for mtIF3, by using the corresponding masks. The P-site was also subjected to focus classification to detect any density of the initiator tRNA, which found out no detectable tRNA occupancy. The two classes, mtSSU-mtIF3 and mtSSU-mtIF3-mtIF3, underwent 3D refinement and postprocessing (Supplementary Table 1). Reported resolutions are based on gold-standard refinement, applying the 0.143 criterion on the FSC between reconstructed half-maps (Supplementary Fig. 2).

To improve the local resolution of mtSSU, four masks were prepared to cover the body core, the head core, tail, and mS39 and performed local-masked 3D refinement (Supplementary Figs. 3a and 4a). To improve the local resolution of the factors, local-masked 3D refinement was also performed using the masks covering the factors and the neighbouring regions (Supplementary Figs. 3b and 4b). Maps were sharpened and filtered by local resolution by using RELION 3.0.

**Model building and refinement.** The models were manually built with Coot<sup>20</sup>. Ligands, metal ions, and modifications were placed based on the density. Hydrogens were generated to have better clash scores. Stereochemical refinement was

performed using phenix.real\_space\_refine in the PHENIX suite<sup>21</sup>. The information on built proteins is in Supplementary Table 2. The final model was validated using MolProbity<sup>22</sup>. Refinement statistics are given in Supplementary Table 1. Figures were generated using PyMOL<sup>23</sup>, UCSF Chimera<sup>24</sup>, and UCSF ChimeraX<sup>25</sup>.

**3D multibody analysis.** 3D multibody analysis was done by RELION 3.0<sup>10</sup>. To analyze the overall conformational change of mtSSU, two masks, head and body masks, were used. The head mask covers the head core and mS39, while the body mask covers the body core and tail as well as the factors (mtIF3 for mtPIC-1 and mtIF2 and mtIF3 for mtPIC-2). Eigenvalues of 100,000 randomly chosen particles are plotted each other for representation. Prior to classification, cleaning was done by removing outliers based on all of the 12 eigenvalues. After cleaning, mtPIC-1 and mtPIC-2 have 371,361 and 99,199 particles, respectively. Particles of mtPIC-1 are classified into three groups based on the eigenvector 1, while those of mtPIC-2 are classified into five groups based on the eigenvectors 1 and 2, as shown in Fig. 4f and Supplementary Fig. 12c.

**Purification of mitoribosomal subunits for in vitro experiments.** Mitoribosomes were purified as previously described<sup>26</sup> with minor modifications. Briefly, HEK293T cells were cultured in 3 L spinner flasks (Corning) in FreeStyle Expression Media (Gibco) until a density of 4 × 10<sup>6</sup> cells/mL, washed with PBS and incubated in swelling buffer (25 mM HEPES-KOH pH 7.5, 100 mM KCl, 20 mM Mg(OAc)<sub>2</sub>, 2 mM DTT) for 20 min at 4 °C. The buffer was then supplemented with sucrose and mannitol to a final concentration of 70 mM and 210 mM, respectively, and the cells were disrupted in a glass homogenizer. The membranes were afterwards centrifuged at 1000 × g for 10 min, the supernatant was collected and centrifuged at 10,000 × g for 10 min. The pellet consisting of crude mitochondria was dissolved in mitochondria isolation buffer (25 mM HEPES-KOH pH 7.5, 100 mM KCl, 20 mM Mg(OAc)<sub>2</sub>, 70 mM sucrose, 210 mM mannitol, 2 mM DTT, supplemented with cOmplete protease inhibitor (Roche)) and treated with 10 U/mL DNase I for 20 min at 4 °C. The mitochondria were then treated with 0.2% digitonin in mitochondria isolation buffer for 5 min and washed two times with mitochondria isolation buffer. Lysis followed, by incubation in lysis buffer (25 mM HEPES-KOH pH 7.45, 100 mM KCl, 20 mM Mg(OAc)<sub>2</sub>, 2% Triton X-100, 2 mM DTT, supplemented with cOmplete protease inhibitor and RNase inhibitor) for 20 min at 4 °C. The membranes were pelleted by centrifugation at 23,500 rpm in a TLA-100.4 rotor for 20 min, and the mitochondrial lysate was then overlaid on top of a 10–30% sucrose gradient prepared in ribosome isolation buffer (25 mM HEPES/KOH pH 7.5, 100 mM KCl, 20 mM Mg(OAc)<sub>2</sub>, 2 mM DTT). The gradient was centrifuged at 21,000 rpm for 16 h in an SW41 Ti rotor, and later fractionated using a Piston Gradient Fractionator (Biocomp). The fractions corresponding to the monosomes were pulled and pelleted by centrifugation at 55,000 rpm in an SW60 rotor. To prepare mitoribosomal subunits, monosomes were incubated in dissociation buffer (20 mM HEPES-KOH pH 7.6, 300 mM KCl, 5 mM MgCl<sub>2</sub>, 1 mM DTT) for 3 h at 4 °C. The sample was then overlaid on top of a 10–30% sucrose gradient prepared in dissociation buffer and ultracentrifuged for 17 h at 21,000 rpm in an SW41 Ti rotor. The gradient was fractionated using a Piston Gradient Fractionator (Biocomp) and the fractions corresponding to mtSSU and mtLSU were pooled and centrifuged at 55,000 rpm in an SW60 rotor for 16 h. The resulting pellets were dissolved in initiation buffer (50 mM Tris-HCl, pH 7.6, 30 mM KCl, 10 mM MgCl<sub>2</sub>, 1 mM DTT, 0.1 mM spermine, 1 mM spermidine) and stored at -80 °C.

**Site-specific labeling of mtIF3.** Labeling of mtIF3 was adapted from previously published protocol<sup>27</sup>, attaching the maleimide functionalized Cy5 fluorophore to the native Cysteine (Cys20). First, the DTT present in the storage buffer was removed by overnight dialysis in labeling buffer (50 mM Tris-HCl pH 7.1, 100 mM NH<sub>4</sub>Cl, 0.1 mM EDTA). Then, disulfide bonds were reduced by incubation in 10-time excess of Tris(2-carboxyethyl)phosphine hydrochloride (TCEP) for 10 min at 37 °C. The labeling reaction was made by incubation of 500 nM mtIF3 with 5-time excess of Cy5-maleimide for 3 h at room temperature. The excess of dye was removed by passing the reaction through two consecutive Zeba<sup>™</sup> Spin Desalting Columns, 7 K MWCO. The labeled mtIF3 was then dialysed against storage buffer (20 mM Tris-HCl pH 7.1, 1 mM EDTA, 10% glycerol, 6 mM β-mercaptoethanol) and stored at -80 °C. The degree of labeling was determined by UV-VIS spectroscopy as 0.75 Cy5 per mtIF3.

**Formation of the preinitiation complex.** Purified mtSSU (150 nM) were incubated with 750 nM mtIF2, 750 nM Cy5-labeled mtIF3, 750 nM Cy3-labeled fMet-tRNA<sup>Met</sup><sub>i</sub>, and 5 mM GTP (in the presence or absence of Atto390-labeled mRNA) in initiation buffer for 15 min at 37 °C and 10 min on ice. The reaction was then overlaid on top of a 10–30% sucrose gradient in Initiation buffer and centrifuged in an SW41 Ti rotor at 21,000 rpm for 17 h. The gradient was afterwards fractionated using a Biocomp Piston Fractionator and the fractions containing mtSSU were pooled and concentrated using Vivaspin 500 centrifugal concentrators up to a volume of 50 μl.

**Formation of the initiation complex.** To assemble the initiation complex, the preinitiation complex was pooled and concentrated to 50 μl using Vivaspin 500



centrifugal concentrators. Afterwards, it was incubated with a stoichiometric amount of mtLSU, 5-time excess of mtIF2, Atto390-labeled mRNA, and 5 mM GTP, in initiation buffer for 15 min at 37 °C. For the mtPIC-1 (Fig. 3a), which did not contain fMet-tRNA<sup>Met</sup>, the reaction was supplemented with a five-time excess of Cy3-labeled fMet-tRNA<sup>Met</sup>. The mixtures were analyzed by sucrose gradient centrifugation. The fractions corresponding to the monosome were pooled and concentrated to 50 µL.

#### Detection and quantification of Atto390-, Cy3-, and Cy5-labeled species.

Fluorescence spectra of Cy3, Cy5, and Atto390 fluorophores were recorded at 25 °C, on a Hitachi Fluorescence Spectrophotometer F-7000, using a 3 mm path length quartz cuvette (105.251-QS, Hellma, Mühlheim, Germany). All spectra were corrected by subtracting the spectra of a reaction in which the nonfluorescent version of the factors (mtIF3, fMet-tRNA<sup>Met</sup>, and mRNA) has been added. The measurements were made using the following settings: Atto390 excitation wavelength 400 nm, emission wavelength 410–650 nm; Cy3 excitation wavelength: 525 nm, emission wavelength: 535–600 nm; Cy5 excitation wavelength: 620 nm, emission wavelength: 625–800 nm.

Calibration curves were made for each of the labeled species, using known concentrations of mtIF3, fMet-tRNA<sup>Met</sup>, and mRNA. Using the calibration curves, we determined the concentrations of Atto390-mRNA, Cy3-fMet-tRNA<sup>Met</sup>, and Cy5-mtIF3 in the initiation reactions from the fluorescence intensity of the samples measured in the same conditions. The calculated concentration of the labeled species was then normalized to the measured concentration of the mtSSU.

For the complete initiation complex, the fraction of monosomes containing bound Cy3-fMet-tRNA<sup>Met</sup> and Atto390-mRNA was not determined due to the low ( $\leq 1$  nM) monosome concentration and therefore variable results.

**Confocal fluorescence detection.** Fluorescence cross-correlation spectroscopy (FCCS) and single-molecule two-color coincidence detection (TCCD) measurements were performed on a MicroTime 200 confocal microscope (PicoQuant, Berlin, Germany) equipped with two pulsed diode lasers of 510 nm (LDH-D-C-510) and 640 nm (LDH-D-C-640) with an average emission power of 25 µW. All measurements were made on PEG-coated glass slides, to eliminate nonspecific interaction of the sample with a glass slide, using labeled molecules in the concentration range of nanomolar for FCCS and picomolar for TCCD.

The initiation reaction was made as described above, using Cy3-fMet-tRNA<sup>Met</sup> and Cy5-mtIF3, in the presence of Atto390-labeled or non-labeled mRNA, and the purified initiation complex was analysed with FCCS. In brief, co-diffusion of mtSSU containing both Cy3 and Cy5 fluorophores would result in correlated signals from the Cy3 and Cy5 channels. On the other hand, signals from separately moving labeled particles result in correlation close to zero. As a positive control, i.e., sample with high double-labeled fraction, a 38-nucleotide single stranded DNA sample, labeled at the 3' end with Cy5 and at the 5' end with Cy3 was purchased from Sigma-Aldrich. Using TCCD (as previously described<sup>28</sup>), we determined that in the positive control, 90% of the molecules carry both fluorophores. In addition, a negative control, i.e., sample with no double-labeled molecule containing a mixture of Cy5-labeled mtIF3 and Cy3-labeled fMet-tRNA<sup>Met</sup> was used.

**In vitro labeling of mitoribosomes at the accessible lysines.** Mitoribosomes (200 nM) were incubated with a 10-time excess (2 µM) of NHS functionalized dyes (Atto488 or Cy5) in Labeling Buffer (50 mM HEPES-KOH pH 7.5, 30 mM KCl, 20 mM MgCl<sub>2</sub>) at 37 °C for 20 min. To purify the labeled ribosomes from the excess of free dye, the labeling reaction was overlaid on top of 1 mL sucrose cushion in Labeling Buffer and centrifuged at 55,000 rpm for 17 h at 4 °C in a TLA-100.4 rotor. The pellet consisting of labeled ribosomes was used fresh for further experiments.

**Double labeling of ribosomes for optical tweezers experiments.** Samples containing pellets of Atto488- and Cy5-labeled mitoribosomes prepared as described above were dissolved in Dissociation Buffer for 3 h at 4 °C, overlaid on top of a 10–30% sucrose gradient prepared in Dissociation Buffer and centrifuged at 21,000 rpm for 17 h at 4 °C in an SW41 Ti rotor. The gradients were then fractionated using a BioComp Fractionator, and the fractions containing the labeled subunits were collected separately and centrifuged at 55,000 rpm for 17 h in an SW60 Ti rotor. The pellet corresponding to Cy5-mtSSU was dissolved in Initiation Buffer and used fresh for optical tweezers experiments. The pellets corresponding to the Atto488 mtSSU and Cy5 mtLSU were dissolved in Reassociation Buffer, mixed in an equimolar ratio and incubated at 4 °C for 1 h to allow the reassociation of the subunits. The sample was then overlaid on top of a 10–30% sucrose gradient and centrifuged at 21,000 rpm for 17 h at 4 °C in an SW41 Ti rotor to separate the reassociated mitoribosomes from the non-reassociated subunits. After fractionation of the gradient, the double-labeled monosomes were pelleted by centrifugation at 55,000 rpm in a TLA-100.4 rotor for 17 h at 4 °C. The resulting pellet was dissolved in Initiation Buffer and used fresh for optical tweezers experiments.

**Preparation of DNA/mRNA constructs for optical tweezers experiments.** The two mRNAs used for optical tweezers experiments were purchased from Eurofins

as DNA/RNA chimeras, containing at the 3' end the cohesive BmtI sequence GATC, followed by the first 58 nucleotides of the native human Cox2 mRNA sequence, and the same sequence without the start codon. Biotinylated lambda DNA was prepared using Klenow Polymerase, biotin-dCTP and biotin dATP as previously described<sup>29,30</sup> and digested with BmtI for 2 h at 37 °C. After gel electrophoresis using a 1% agarose gel, the 35 kbp construct was purified and ligated with the DNA/RNA chimeras for 1 h at room temperature. The ligated product was separated with gel electrophoresis, purified and stored at 4 °C no longer than two days, in the presence of RNase inhibitors.

**Single-molecule imaging in an optical tweezer setup.** Optical tweezer experiments were performed on C-Trap<sup>TM</sup> system integrating optical tweezers, confocal fluorescence microscopy, and microfluidics and recorded using BlueLake software (LUMICKS B.V., the Netherlands). Initiation reactions were made by incubating 200 nM double-labeled ribosomes or Cy5-labeled mtSSU, 240 nM mtIF3, 240 nM mtIF2, 240 nM fMet-tRNA<sup>Met</sup>, and 400 nM biotinylated DNA/RNA construct in Initiation Buffer for 2 h at 37 °C. Tether formation was performed in situ (inside the laminar flow cell chamber, LUMICKS) by trapping 4.47 µm streptavidin-coated polystyrene beads with optical traps in Channel 1 and bringing beads in contact with DNA/RNA constructs, preincubated with proteins, in Channel 2. Binding of the complete mitoribosome or the small subunit to RNA was detected by dual-color imaging with 532 nm and 638 nm lasers in Initiation Buffer (Channel 3). Images were further converted to \*.tiff and analyzed with an open source Java image processing program ImageJ (<https://imagej.net/ImageJ>).

**Reporting summary.** Further information on research design is available in the Nature Research Reporting Summary linked to this article.

#### Data availability

The data that support this study is available from the corresponding authors upon reasonable request. The cryo-EM maps have been deposited in the Electron Microscopy Data Bank with accession codes EMD-10021, EMD-10022, EMD-10023, EMD-10024, EMD-10025, EMD-10026, EMD-10027, EMD-10028, EMD-10029, EMD-10030, EMD-10031 and EMD-10032. The atomic models have been deposited in the Protein Data Bank under accession codes PDB 6RW4 and PDB 6RW5. The data source behind Fig. 6d, Supplementary Fig. 9a, b and Supplementary Table 4 are provided as a Source Data file.

Received: 16 March 2020; Accepted: 7 May 2020;

Published online: 10 June 2020

#### References

- Amunts, A., Brown, A., Toots, J., Scheres, S. H. W. & Ramakrishnan, V. The structure of the human mitochondrial ribosome. *Science* **348**, 95–98 (2015).
- Greber, B. J. et al. The complete structure of the 55S mammalian mitochondrial ribosome. *Science* <https://doi.org/10.1126/science.aaa3872> (2015).
- Kummer, E. et al. Unique features of mammalian mitochondrial translation initiation revealed by cryo-EM. *Nature* **560**, 263–267 (2018).
- Rudler, D. L. et al. Fidelity of translation initiation is required for coordinated respiratory complex assembly. *Sci. Adv.* **5**, eaay2118 (2019).
- Hussain, T., Llácer, J. L., Wimberly, B. T., Kieft, J. S. & Ramakrishnan, V. Large-scale movements of IF3 and tRNA during bacterial translation initiation. *Cell* <https://doi.org/10.1016/j.cell.2016.08.074> (2016).
- Sacerdot, C. et al. Mutations that alter initiation codon discrimination by *Escherichia coli* initiation factor IF3. *J. Mol. Biol.* <https://doi.org/10.1006/jmbi.1999.2737> (1999).
- Maar, D. et al. A single mutation in the IF3 N-terminal domain perturbs the fidelity of translation initiation at three levels. *J. Mol. Biol.* <https://doi.org/10.1016/j.jmb.2008.09.012> (2008).
- Koripella, R. K. et al. Structure of human mitochondrial translation initiation factor 3 bound to the small ribosomal subunit. *iScience* <https://doi.org/10.1016/j.isci.2018.12.030> (2019).
- Julián, P. et al. The cryo-EM structure of a complete 30S translation initiation complex from *Escherichia coli*. *PLoS Biol.* <https://doi.org/10.1371/journal.pbio.1001095> (2011).
- Zivanov, J. et al. New tools for automated high-resolution cryo-EM structure determination in RELION-3. *elife* <https://doi.org/10.7554/eLife.42166> (2018).
- Koc, E. C. et al. Identification and characterization of CHCHD1, AURKAIP1, and CRIF1 as new members of the mammalian mitochondrial ribosome. *Front. Physiol.* <https://doi.org/10.3389/fphys.2013.00183> (2013).
- Simonetti, A. et al. Involvement of protein IF2 N domain in ribosomal subunit joining revealed from architecture and function of the full-length initiation factor. *Proc. Natl Acad. Sci. USA* **110**, 15656–15661 (2013).

13. Gaur, R. et al. A single mammalian mitochondrial translation initiation factor functionally replaces two bacterial factors. *Mol. Cell* **29**, 180–190 (2008).
14. Yassin, A. S. et al. Insertion domain within mammalian mitochondrial translation initiation factor 2 serves the role of eubacterial initiation factor 1. *Proc. Natl Acad. Sci. USA* **108**, 3918–3923 (2011).
15. Udagawa, T., Shimizu, Y. & Ueda, T. Evidence for the translation initiation of leaderless mRNAs by the intact 70 S ribosome without its dissociation into subunits in Eubacteria. *J. Biol. Chem.* <https://doi.org/10.1074/jbc.M308784200> (2004).
16. Moll, I., Hirokawa, G., Kiel, M. C., Kaji, A. & Bläsi, U. Translation initiation with 70S ribosomes: an alternative pathway for leaderless mRNAs. *Nucleic Acids Res.* **32**, 3354–3363 (2004).
17. Pan, D., Qin, H. & Cooperman, B. S. Synthesis and functional activity of tRNAs labeled with fluorescent hydrazides in the D-loop. *RNA* <https://doi.org/10.1261/rna.1257509> (2009).
18. Zheng, S. Q., Palovcak, E., Armache, J.-P., Cheng, Y. & Agard, D. A. Anisotropic correction of beam-induced motion for improved single-particle electron cryo-microscopy. *bioRxiv* <https://doi.org/10.1101/061960> (2016).
19. Zhang, K. Gctf: Real-time C. T. F. determination and correction. *J. Struct. Biol.* <https://doi.org/10.1016/j.jsb.2015.11.003> (2016).
20. Emsley, P., Lohkamp, B., Scott, W. G. & Cowtan, K. Features and development of Coot. *Acta Crystallogr. Sect. D. Biol. Crystallogr.* **66**, 486–501 (2010).
21. Adams, P. D. et al. PHENIX: a comprehensive Python-based system for macromolecular structure solution. *Acta Crystallogr. Sect. D. Biol. Crystallogr.* **66**, 213–221 (2010).
22. Chen, V. B. et al. MolProbity: all-atom structure validation for macromolecular crystallography. *Acta Crystallogr. Sect. D. Biol. Crystallogr.* <https://doi.org/10.1107/s0907444909042073> (2010).
23. DeLano, W. L. PYMOL: an open-source molecular graphics tool. *CCP4 Newslett Protein Crystallogr* **40**, 11 (2002).
24. Pettersen, E. F. et al. UCSF Chimera—a visualization system for exploratory research and analysis. *J. Comput. Chem.* <https://doi.org/10.1002/jcc.20084> (2004).
25. Goddard, T. D. et al. UCSF ChimeraX: meeting modern challenges in visualization and analysis. *Protein Sci.* <https://doi.org/10.1002/pro.3235> (2018).
26. Aibara, S., Andréll, J., Singh, V. & Amunts, A. Rapid isolation of the mitoribosome from HEK cells. *J. Vis. Exp.* <https://doi.org/10.3791/57877> (2018).
27. Milon, P. et al. Transient kinetics, fluorescence, and FRET in studies of initiation of translation in bacteria. *Methods Enzymol.* [https://doi.org/10.1016/S0076-6879\(07\)30001-3](https://doi.org/10.1016/S0076-6879(07)30001-3) (2007).
28. Kempf, N. et al. A novel method to evaluate ribosomal performance in cell-free protein synthesis systems. *Sci. Rep.* **7**, <https://doi.org/10.1038/srep46753> (2017).
29. Baker, N. A., Sept, D., Joseph, S., Holst, M. J. & McCammon, J. A. Electrostatics of nanosystems: application to microtubules and the ribosome. *Proc. Natl Acad. Sci. USA* <https://doi.org/10.1073/pnas.181342398> (2001).
30. Smith, S. B., Cui, Y. & Bustamante, C. Overstretching B-DNA: The elastic response of individual double-stranded and single-stranded DNA molecules. *Science.* <https://doi.org/10.1126/science.271.5250.795> (1996).

## Acknowledgements

We thank B.S. Cooperman for providing fMet-tRNA<sup>Met</sup>, aminoacylated, formylated and labeled with the Cy3 fluorophore; M. Rodnina for providing the unlabeled fMet-tRNA<sup>Met</sup>, aminoacylated and formylated; A. Mukhortova and J. Andrecka (Lumicks) for

help with optical tweezers experiments; R. Kock Flygaard and A. Perez Boerema for help with figures; and T. Hussain for critical reading of the manuscript. This work was supported by H2020-MSCA-ITN-2015 (00579), Swedish Foundation for Strategic Research (FFL15:0325), Ragnar Söderberg Foundation (M44/16), Swedish Research Council (NT\_2015-04107), Cancerfonden (2017/1041), European Research Council (ERC-2018-StG-805230), Knut and Alice Wallenberg Foundation (2018.0080), Karolinska Institute and Max Planck Institute. Y.I. is a recipient of H2020-MSCA-IF-2017 (799399-Itohibo), A.A. is EMBO Young Investigator Fellow, J.R. is the Fellow of the Knut and Alice Wallenberg Foundation. H.H. and O.Y. acknowledge support by the International Helmholtz Research School of Biophysics and Soft Matter. The cryo-EM data were collected at SciLifeLab cryo-EM facility funded by the Knut and Alice Wallenberg, Family Erling Persson, and Kempe foundations. Open access funding provided by Karolinska Institute.

## Author contributions

J.R. and A.A. designed the study. A.K. prepared the sample for cryo-EM. Y.I. performed cryo-EM data collection, processing, and model building. C.R., H.S., J.R., O.Y., and H.H. performed fluorescence analysis. A.K., Y.I., C.R., J.R., and A.A. wrote the manuscript. All authors discussed and commented on the final manuscript.

## Competing interests

The authors declare no competing interests.

## Additional information

**Supplementary information** is available for this paper at <https://doi.org/10.1038/s41467-020-16503-2>.

**Correspondence** and requests for materials should be addressed to A.A. or J.R.

**Peer review information** *Nature Communications* thanks Sebastian Klinge, Bob Lightowers and the other, anonymous, reviewer(s) for their contribution to the peer review of this work. Peer reviewer reports are available.

**Reprints and permission information** is available at <http://www.nature.com/reprints>

**Publisher's note** Springer Nature remains neutral with regard to jurisdictional claims in published maps and institutional affiliations.



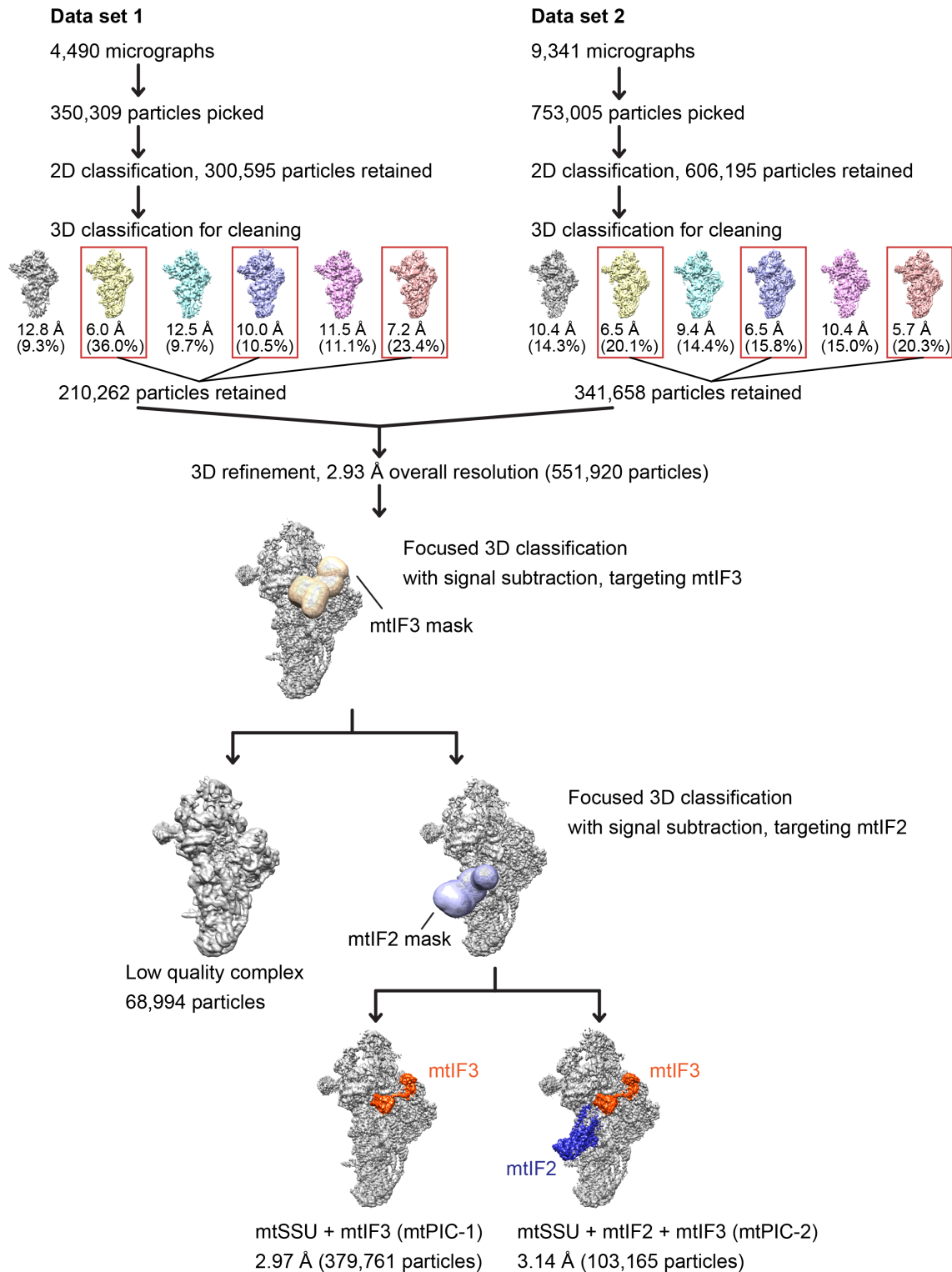
**Open Access** This article is licensed under a Creative Commons Attribution 4.0 International License, which permits use, sharing, adaptation, distribution and reproduction in any medium or format, as long as you give appropriate credit to the original author(s) and the source, provide a link to the Creative Commons license, and indicate if changes were made. The images or other third party material in this article are included in the article's Creative Commons license, unless indicated otherwise in a credit line to the material. If material is not included in the article's Creative Commons license and your intended use is not permitted by statutory regulation or exceeds the permitted use, you will need to obtain permission directly from the copyright holder. To view a copy of this license, visit <http://creativecommons.org/licenses/by/4.0/>.

© The Author(s) 2020

## **SUPPLEMENTARY INFORMATION**

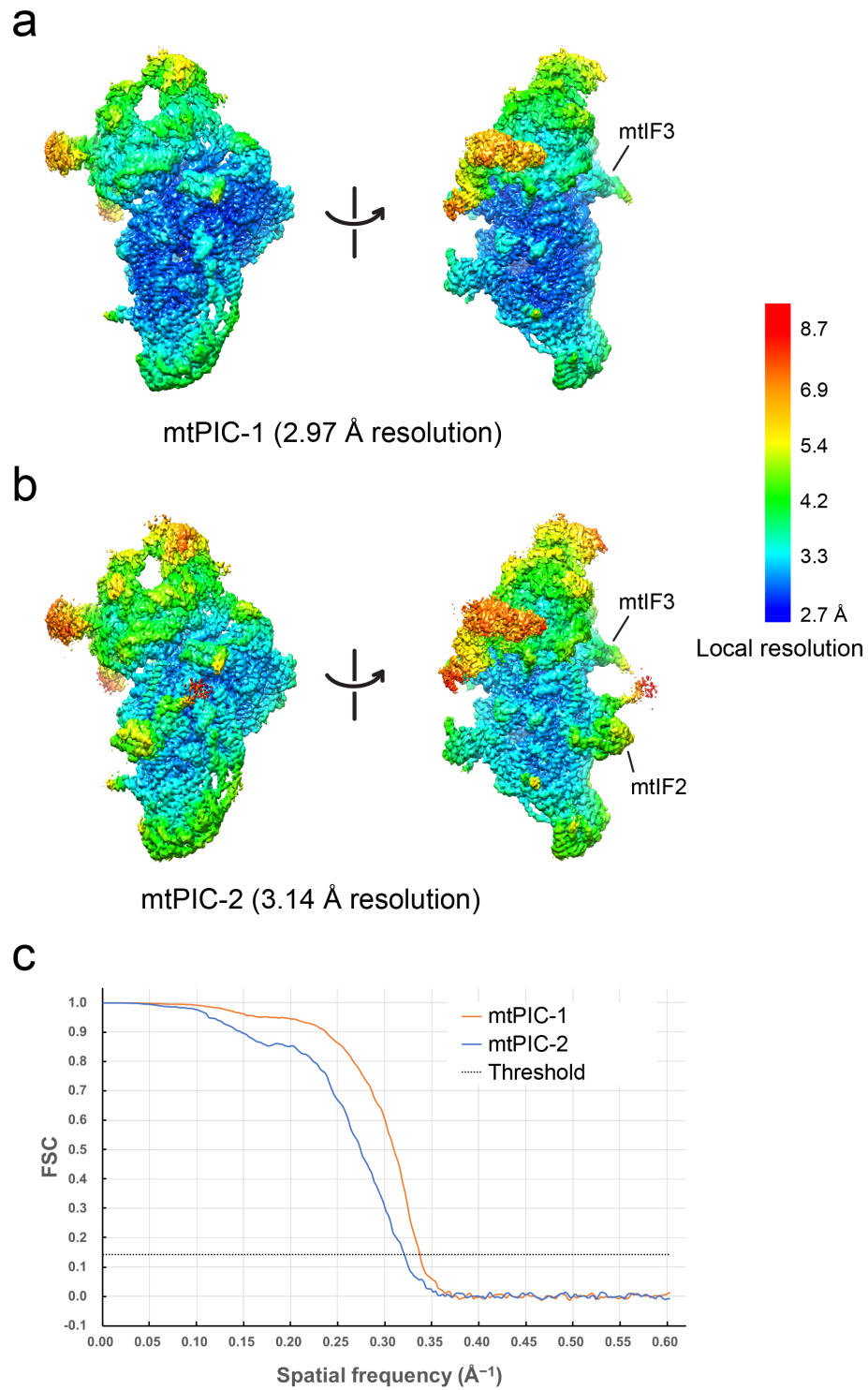
### **Distinct pre-initiation steps in human mitochondrial translation**

Khawaja, Itoh et al.



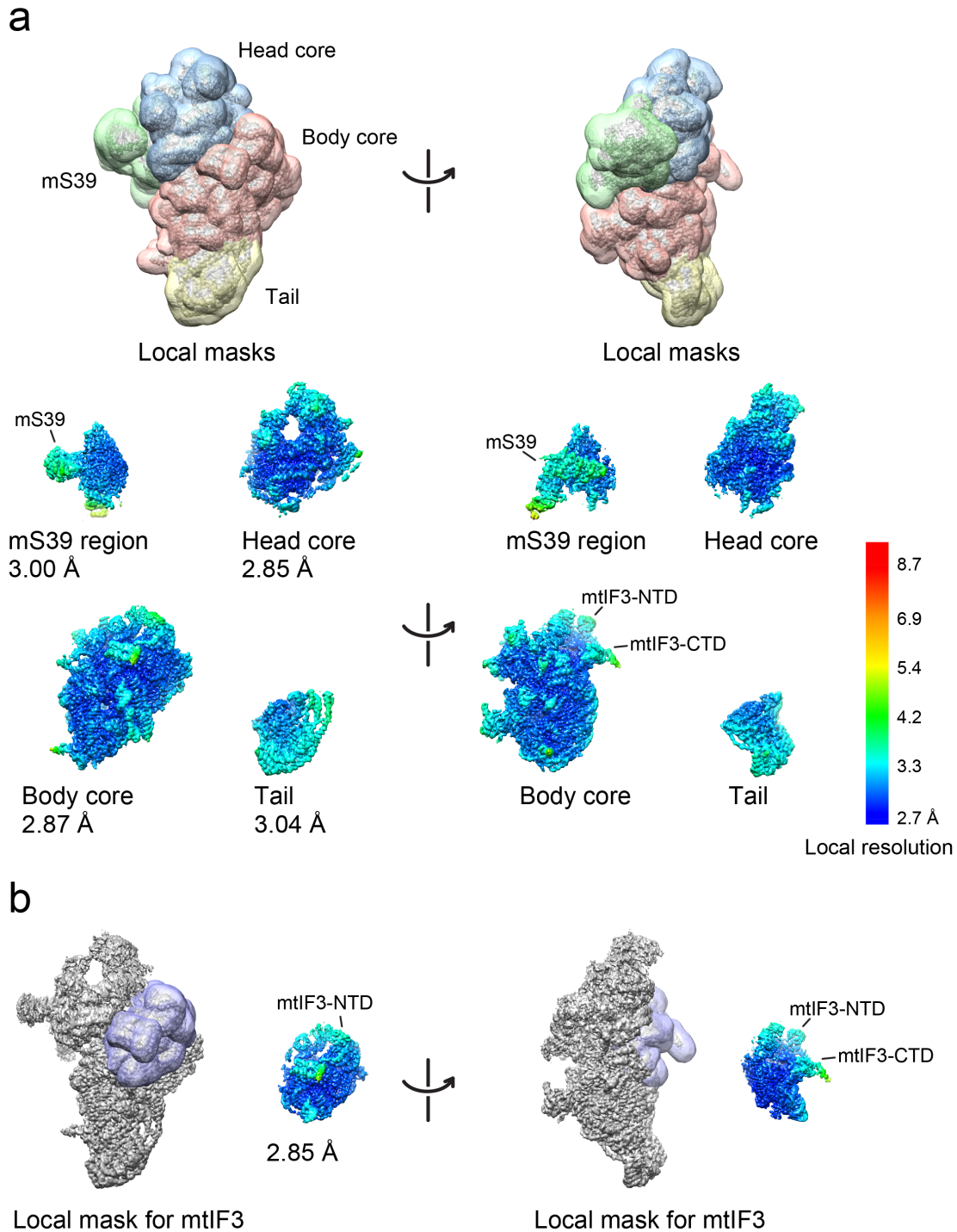
**Supplementary Figure 1. Data processing overview.**

Two data sets were processed separately up to 3D classification for cleaning. After merging the data and 3D refinement, two steps of focused 3D classification with signal subtraction were performed by using mtIF3 and mtIF2 masks to separate the mtIF3-only and mtIF2-mtIF3 bound complexes.



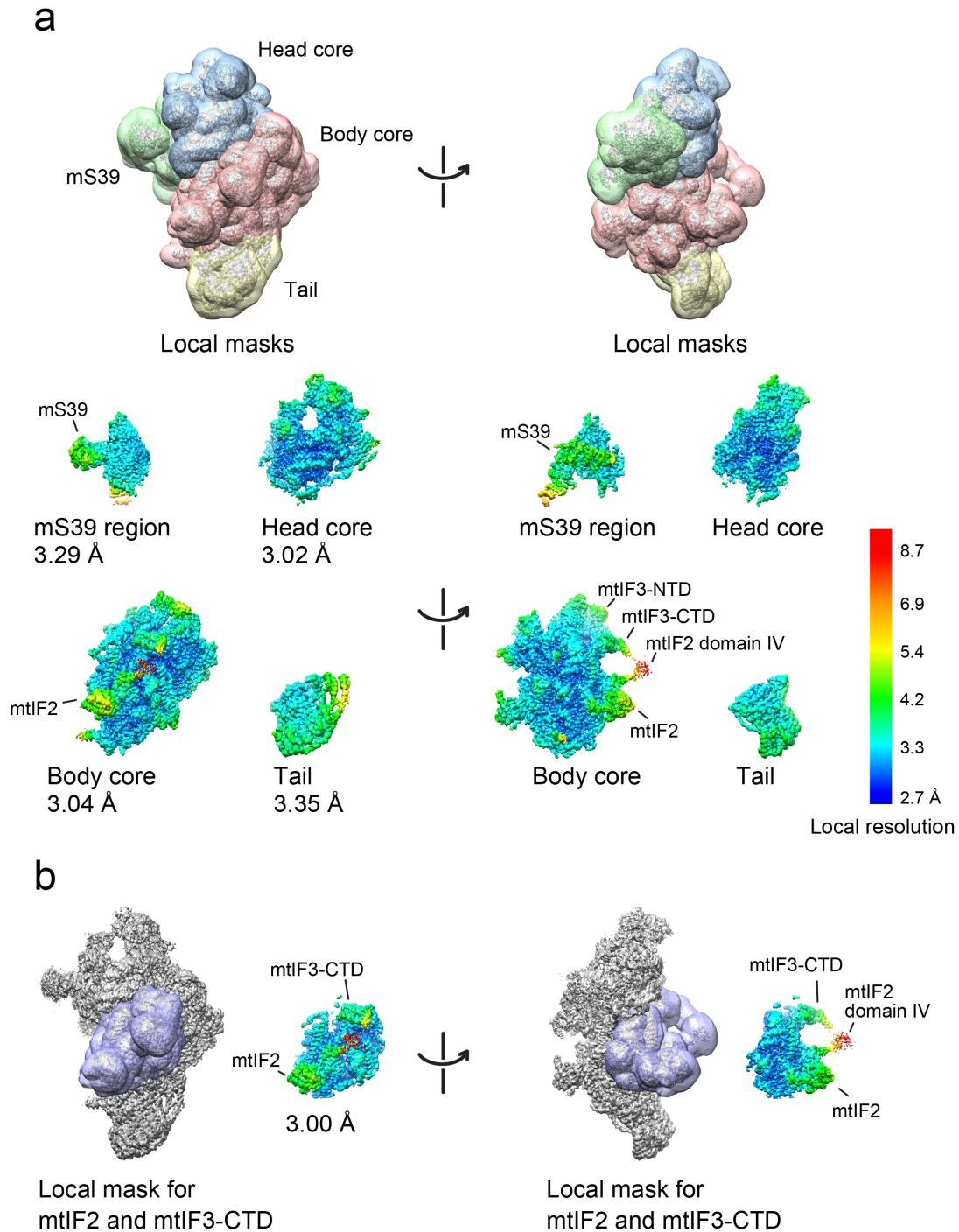
**Supplementary Figure 2. Resolution of the maps.**

**a,b** Local resolution was estimated by Relion 3 and presented by color gradation on the surfaces of the unsharpened overall maps of mtPIC-1 (**a**) and mtPIC-2 (**b**). **c** Gold-standard Fourier shell correlation (FSC) curves of the maps were colored orange (mtPIC-1) and blue (mtPIC-2), respectively with the threshold 0.143.



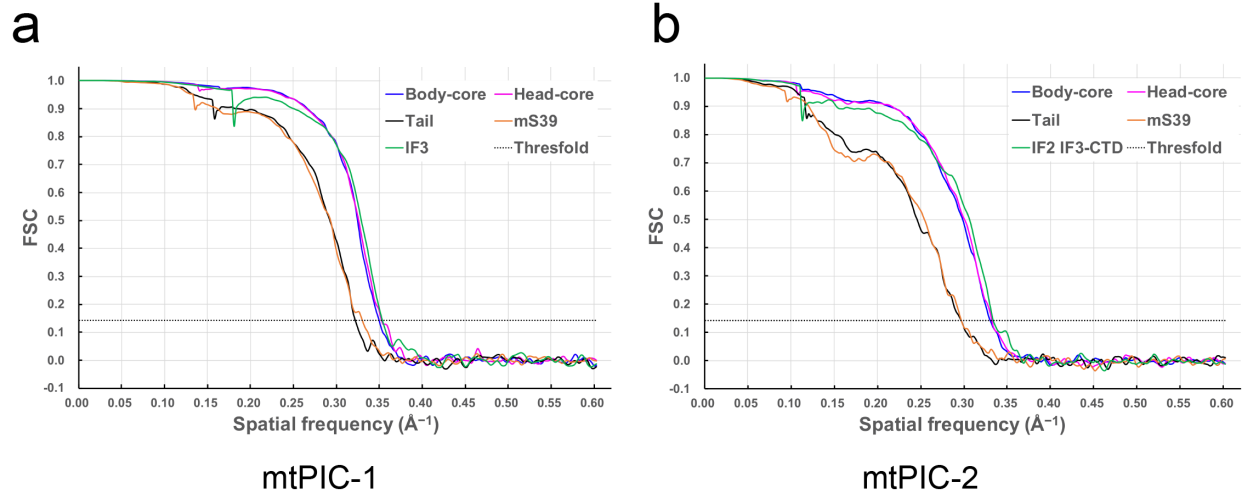
**Supplementary Figure 3. Local masked refinement of mtPIC-1.**

**a** Four local masks covering the body core, the head core, tail, and the mS39 region, respectively, were prepared and used for local 3D refinement to improve the local resolution. Local resolution was estimated by Relion 3 and presented by color gradation on the surfaces of the unsharpened maps. **b** A local mask covering mtIF3 and its neighboring was prepared to improve the local resolution of mtIF3. The resulting local resolution is shown.



**Supplementary Figure 4. Local masked refinement of mtPIC-2.**

**a** Four local masks covering the body core, the head core, tail, and the mS39 region, respectively, were prepared and used for local 3D refinement to improve the local resolution. Local resolution was estimated by Relion 3 and presented by color gradation on the surfaces of the unsharpened maps. **b** A local mask covering mtlF2, mtlF3-CTD, and its neighboring was prepared to improve the local resolution of mtlF2 and mtlF3-CTD. The resulting local resolution is shown.

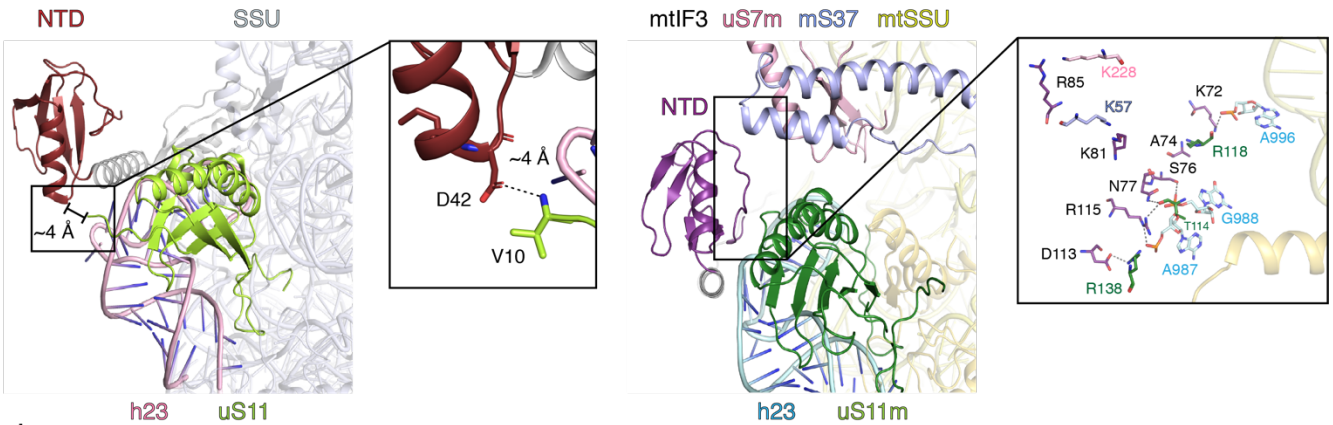


**Supplementary Figure 5. FSC curves of the local masked refined maps.**

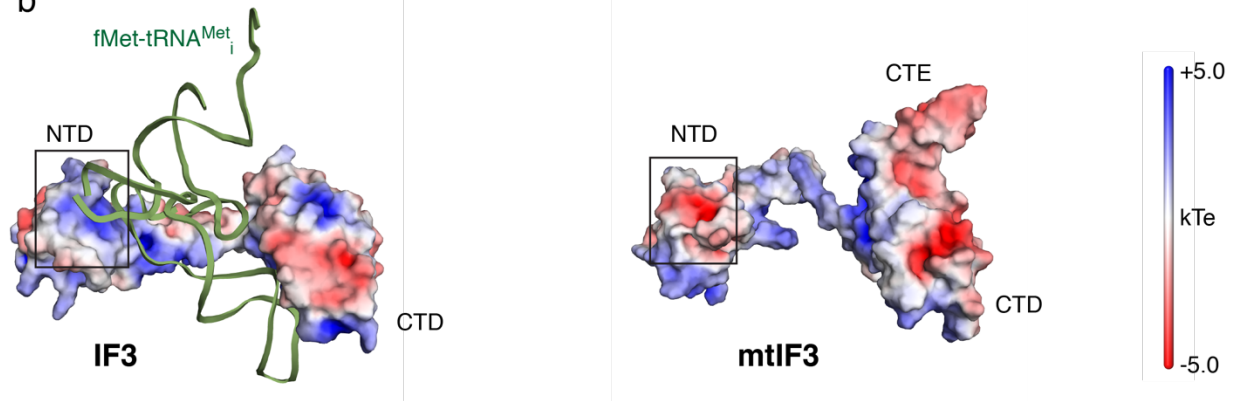
Gold standard FSC curves of the local masked refined maps for mtPIC-1 (a) and mtPIC-2 (b) are shown with the threshold 0.143.



a



b



c

Homo sapiens	MAALFLKRLTLTQT-VKSEN--SCIRCFGKHILQKTAPAQLSPI--ASAPRLSFLIHAKAFS--TAEDTONEGKK	67
Sus scrofa	MAALFLKRLTLTQTIRTEFS--CTARCLGERVVGQKTSPPAPPV---ASAPRPSCLIHAKAFS--TE-DTQERKK	67
Mus musculus	M-AVLLMRLMLQTKLDHN--LIGRCLQRHAV-KPDDPAQLSLS--ASTPKLLYLTSAGKFS--TAGDPQGERRQ	67
Rattus norvegicus	M-AVLLKRLMPQAMKTDSS--LLRRCFRRHTV-KPDLARPSLT---ASTPKLLHLISAKGFS--TVGDTGERRQ	67
Danio rerio	---MSLGLVKLFLLSRSTFRPISRLNLLPLTKPPTLRPARGCQIFLPWPRAFSTDTDDGGDPAIQTDSQKKKNKKL	72
R. felis	-----	0
E. coli	-----mkggkr	6
T. thermophilus	-----	0
M. smegmatis	-----mgllvrpnig	10

Homo sapiens	TKKNTAFSNVGRKISORVILFDEKGNLGNMHRANVIRLMDERDLRVLVQNTSTPEAEYQLMGLGQILQERQR	142
Sus scrofa	KKKDETAFSNIGRKHIERIIFVLDEQGNLGHMHRANVIRLMAERDLRLVRRDPGAEPFQYQLLTGAQIHOERLR	142
Mus musculus	KRR--DAFSNTGRKISERIRVLDKGMDLGMMHRADVIRLMNKQDLRLVQNTSPEPEYQLMTGQIHOERLR	140
Rattus norvegicus	KRR--DAFSNTGRKISERIRVLDKGVLDGTMHRADVIRLMDKQDLRLVQNTSPEPEYQLMTGQIHOERLR	140
Danio rerio	DPRARVTISSVGRKIGQRHIIHLIGADGEDLVGKHRADVIRLLDQTLKLVAVNDSRDPVYKLMKGEIHEEQLK	147
R. felis	-----mgvvnirkaldmaerasldlvespnavppvcildfkgkfyekkk	47
E. coli	vq--tarphringeiraqevltglegeelgivslrealekaeeaaqdlvespnaeppvcimdygkflyeksk	79
T. thermophilus	----MKEYLTNERITRAKQVAVVGGPDGKQIGIMDTREALRLAQEMLDLVLVGNADPPVARIMDYKWRVEQGM	70
M. smegmatis	gp--istetrvnerirvpevliligpggeevgviriedalrvaadaaldlveapnarppvcimdygkykyaq	83

Homo sapiens	IREMEKANPKT-GPTLRKELIISNIGQHDLDTKTKIQQWIKKKHLVQITIKKGNVDVSENEEMEIFHQILQTM	217
Sus scrofa	LRERAGRAEPPK-GPTLTKELFSSNIGQHDLDTKSKQIQQWIEKKYHVQVITIKKGRNABEPENKMEELCNQILQTM	217
Mus musculus	LRERQEKAKPKT-GPTMTKELVFSSNIGQHDLDTKSKQIQQWIEKKYHVQVITIKKRDABEQSEETEEIFNQILQTM	215
Rattus norvegicus	LRERQEKAKPKTAGPTVTKELIFSSNIGQHDLDTKSKQIQQWIEKKYHVQVITIKKRDABEQSGEMDEIFNQILQTM	216
Danio rerio	LRERKQDKKGV---VQSKELNFSISLHLDLNRKLRQIVSWLEKNNHVKLTIRAGTNSPTLDKILQTMVE--KI	231
R. felis	rlhe---arkkqkivvlkemfkpnisigdfetklrkikeflkdgdvkwiswfkgreilhkevgqelfkrievgl	120
E. coli	sake---qkkkqvivqkeikfzptdegyqvlrrelirfleegdkakitlfrfgremahqqigmevlrvnkddl	152
T. thermophilus	AEKE---ARKKAKRTEVSKIFRVKIDEDHYDQTKLGHIKRFLQEGHKVKVTIMFRGDEVVHPELGERILNRVTEDL	143
M. smegmatis	kaire---srknqqqtvvkeqklrpkigdhdyetkkgvirlleagskvktimfrgeqspeligyrlqlqadv	156

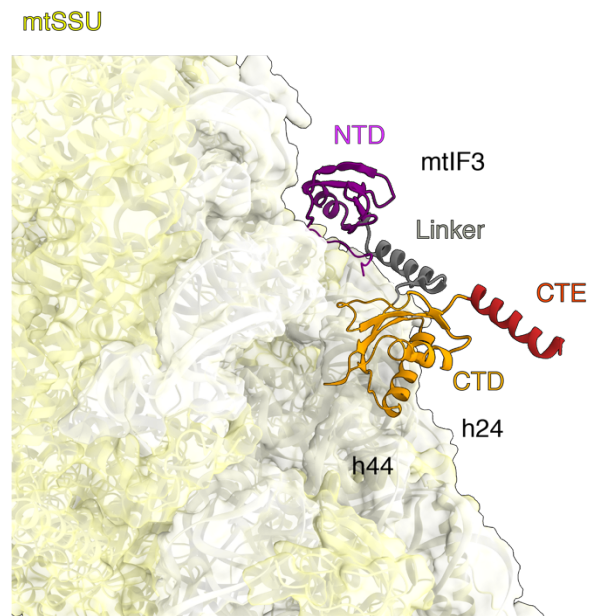
  

Homo sapiens	PGIATFSSRPQAVQGGKALMCVLRRAFSGGKALMCVLRRAFSKNEEKAYKETOETQERDTLN--KDHGNDKESNVLHQ	278
Sus scrofa	PGIATFSSRPQLIRGGKAMMCVLRPLSGGKAMMCVLRPLSRKEE-ANRAAQGPPRGDPLS--REDGNHGASDVLHQ	277
Mus musculus	PDIAFSSRPKAIIRGGTASMCVFRHLGGTASMCVFRHLSSKKEEKAYRESQESQRDDTLS--KDDGNSKESDVLVCC	276
Rattus norvegicus	PGIATFLSRPKAVIRGGTASMCVFRHVSGGTASMCVFRHVSKEEKAYRESQESQKGDITLS--KDDRSNKSVDLVC	276
Danio rerio	SVPVAVFVSNPPLIRGGASMCIFRLASGGGRASMCIFRLASAKEQ-QKETLKKKADSVEEGQSDAAGGTEETKDLKQQ	280
R. felis	egpikidqha-kmegkqmimivspdi-kv-----	147
E. coli	qelavvesfptkiegrqmivlapkk-kq-----	183
T. thermophilus	KDLAVVEMKP-EMLGRDMNMLLAPVK-gsa-----	171
M. smegmatis	aeygfvetsa-kqdgrrnmtvmlaphr-vaktakraaaeqaerpggp-----apdedas-----	210

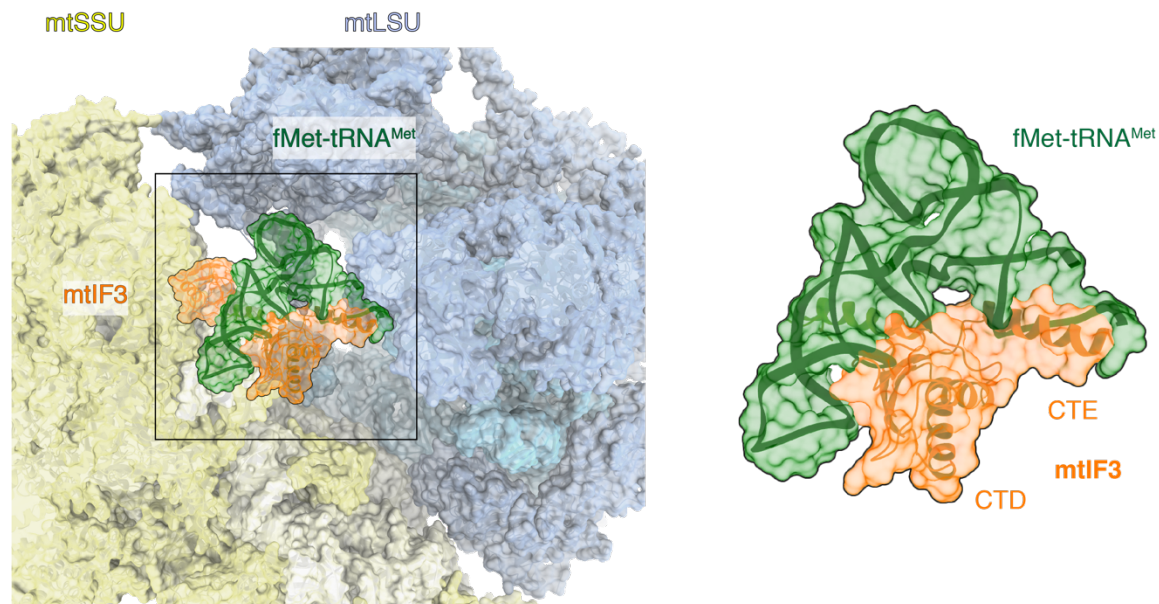
### Supplementary Figure 6. Comparison with bacterial IF3.

**a** Comparison of the IF3 NTD and the small ribosomal subunit interactions. IF3-NTD of the bacterium *Thermus thermophilus* makes a possible interaction with the uS11 (green) of SSU (PDB; 5LMN). The closest distance between residues of the NTD (D41) and uS11 (V10) is marked. In contrast, mtIF3 is associated to the mtSSU platform through several interactions with h23 (cyan) of 12S rRNA and uS11m (dark green, in close proximity to uS7m (pink) and mS37 (blue)). **b** Comparison of the electrostatic potential on the surfaces of the bacterial IF3 (PDB: 5LMS, shown with fMet-tRNA<sup>Met<sub>i</sub></sup>) and mtIF3. Electrostatic potential was calculated by using ABPS<sup>29</sup>. Electronegative and electropositive regions are colored in red and blue, respectively. The binding site of the IF3-NTD with the elbow of fMet-tRNA<sup>Met<sub>i</sub></sup> is marked by a rectangle. **c** Sequence alignment of the human mtIF3 with its vertebrate and bacterial orthologs. The human mtIF3 sequence is color-coded corresponding to its domain organization (NTE; turquoise, NTD; purple, CTD; yellow, CTE; red). Green and orange columns indicate the binding sites of mtIF3 with the mtSSU. The green columns represent mtIF3 residues which are not conserved while the orange columns display the conserved residues. The pink columns show residues involved in the tRNA discrimination in bacteria (G71 and Y75), which are not conserved in vertebrates. Residues that bind the elbow of initiator tRNA in bacteria are displayed in blue.

a



b

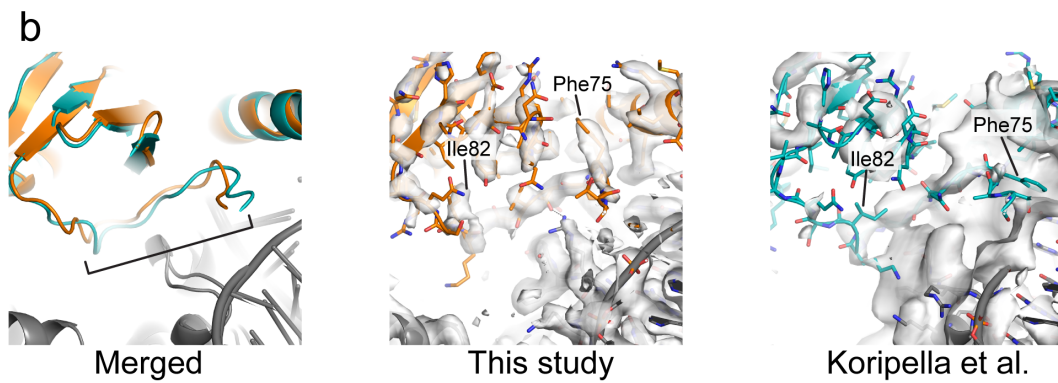


**Supplementary Figure 7. The mtIF3-CTE prevents binding of the fMet-tRNA<sup>Met<sub>i</sub></sup> to the mtSSU.**

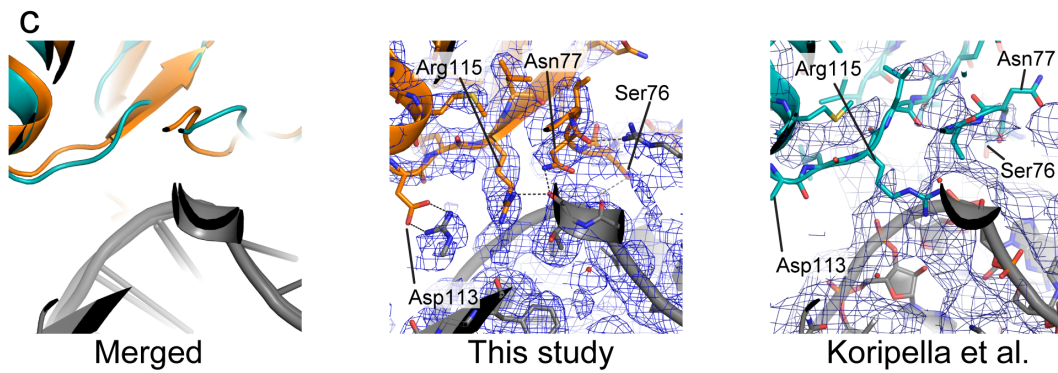
**a** The mitochondrial specific mtIF3-CTE forms a helix facing outward from the mtSSU. **b** The mtIF3-CTE occupies the region of the fMet-tRNA<sup>Met<sub>i</sub></sup> acceptor stem binding site shown by superposition with the complete initiation complex (PDB: 6GAW). The transparent surface and ribbon representation of the factors (right panel) illustrate the clash of mtIF3-CTD and CTE with fMet-tRNA<sup>Met<sub>i</sub></sup> indicative of their alternate association to the mtSSU.



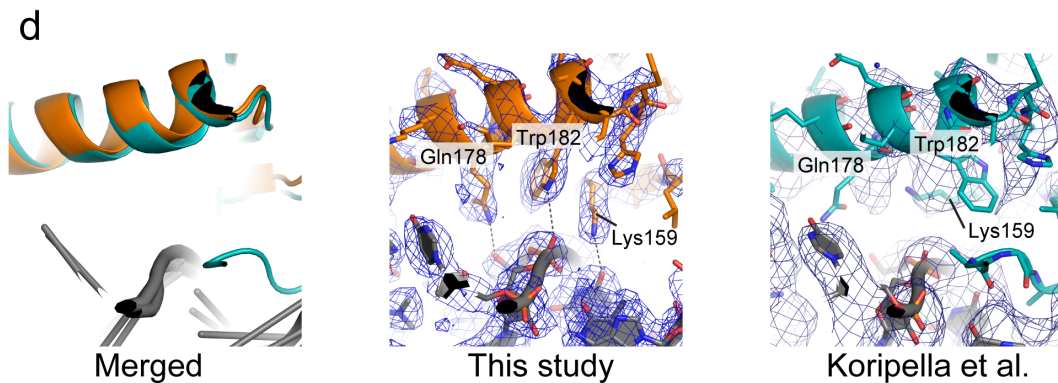
**NTE of mtIF3**



**The residues 75–82 in NTD of mtIF3**



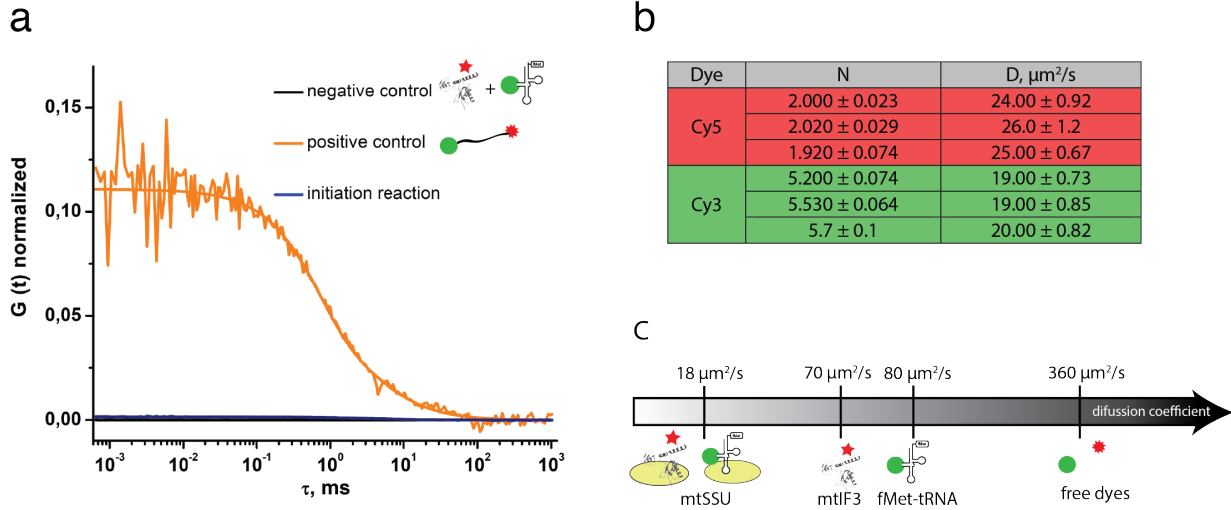
**mtIF3 NTD and mtSSU interactions**



**mtIF3 CTD and mtSSU interactions**

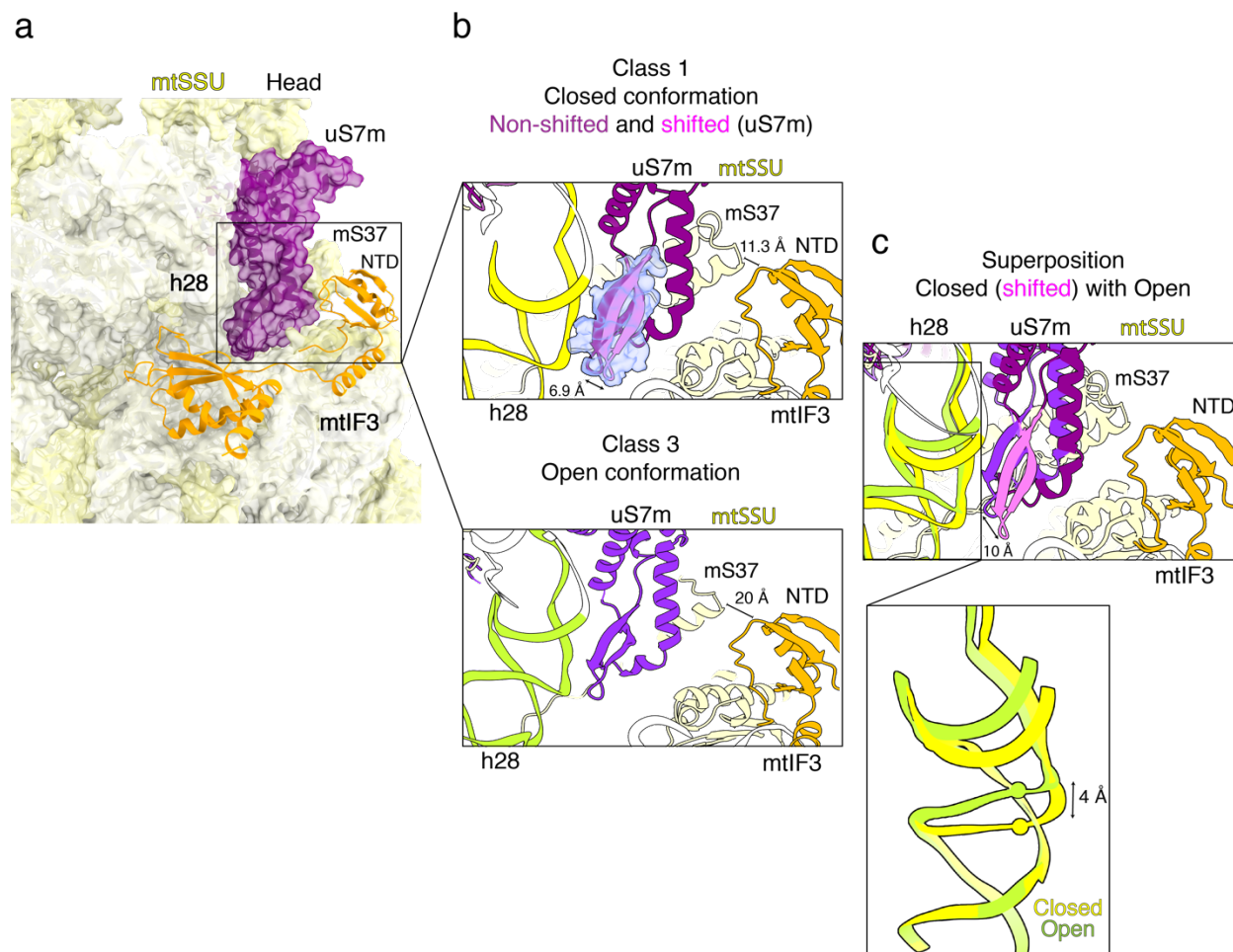
**Supplementary Figure 8. Comparison of the mtIF3-mtSSU interactions between this study and Koripella et al. <sup>6</sup>.**

**a** The NTE of mtIF3 modeled in Koripella et al.<sup>6</sup>. The merged structures of mtIF3 from this report (orange) and from Koripella et al. (green cyan) are shown in the left panel. The structures are superposed by using the densities of the mtSSU body for fitting. The cryo-EM densities of this report (middle panel) and Koripella et al. (right panel, EMD-9358) are shown as surface with the contour levels of 6.0 and 3.6, respectively. The NTE is modeled only in Koripella et al., whereas it is missing in our model. There is no significant density of the NTE in either of the maps. **b** The loop consists of the residues 75–82 in NTD. Superposed ribbon models (left panel) and additional stick models with the cryo-EM densities of this report (middle panel) and Koripella et al. (right panel) are shown with the contour levels of 5.0 and 3.0, respectively. In our model, all side chains in this region are supported by the density, while some of the side chains do not agree with the density in Koripella et al. This causes the different interpretation of the interactions between the mtIF3-NTD and the mtSSU. **c** Picked-up interactions between the mtIF3-NTD and the mtSSU. Merged ribbon model (left panel) and the individual stick models with polar interactions (middle and right panels) are shown. The cryo-EM densities are shown as mesh with the contour levels of 5.0 and 3.0, respectively in the middle and right panels. Ser76, Asn77, Arg111, and Asp113 are interacting in our model, whereas they are away from the mtSSU in Koripella et al. **d** Picked-up interactions between the mtIF3 CTD and the mtSSU. Merged ribbon model (left panel) and the individual stick models and polar interactions (middle and right panels) are shown. The cryo-EM densities are shown as mesh with the contour levels of 9.0 and 6.0, respectively in the middle and right panel. Interactions through Lys159, Gln178, and Trp182 are supported by the density in our model. In Koripella et al., the Gln178 side chain is out of the density, the Lys159 side chain occupies the density for Trp182 and the Trp182 side chain is kicked out.



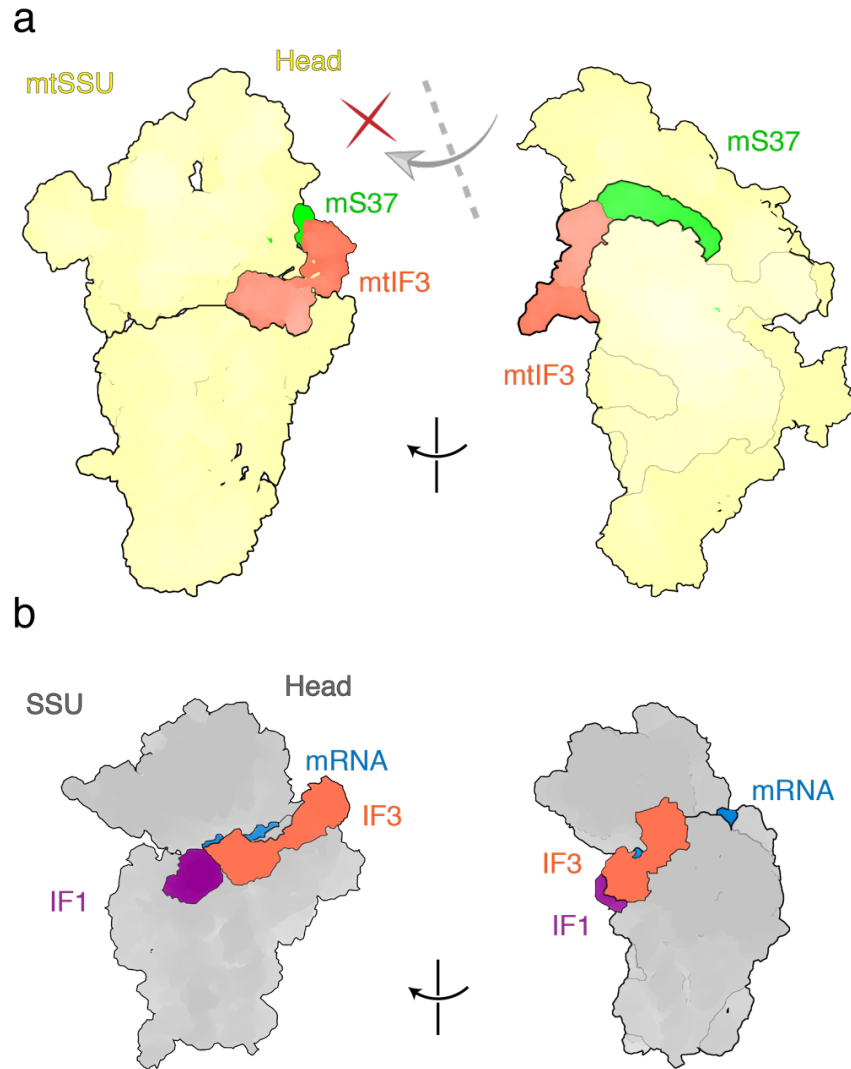
**Supplementary Figure 9. Fluorescence cross-correlation spectroscopy measurements of the mtPIC formed with Cy3-fMet-tRNA<sup>Met<sub>i</sub></sup> and Cy5-mtIF3.**

**a** Cross-correlation curves normalized to concentration, for the mtPIC (blue curve), negative control – a mixture of Cy5-mtIF3 and Cy3-fMet-tRNA<sup>Met<sub>i</sub></sup> (black curve) and positive control – a 38-nucleotide DNA labeled with Cy3 at the 3' end and with Cy5 at the 5' end (orange curve). **b** Diffusion coefficients of the Cy3 and Cy5 labeled species during the measurement time of 15 minutes show a constant value of  $20 \mu\text{m}^2/\text{s}$ , proving that the labeled mtIF3 and fMet-tRNA<sup>Met<sub>i</sub></sup> do not dissociate from the complex formed with the mtSSU. Diffusion coefficients for Cy3 and Cy5 channels show slightly different values due to mismatch of the green and red detection volumes in confocal microscope. **c** Expected diffusion coefficients of the participating labeled species. Source data are provided as a Source Data file.



**Supplementary Figure 10. Conformations of the h28-associated region of uS7m during the mtSSU head movement of the mtPIC-1.**

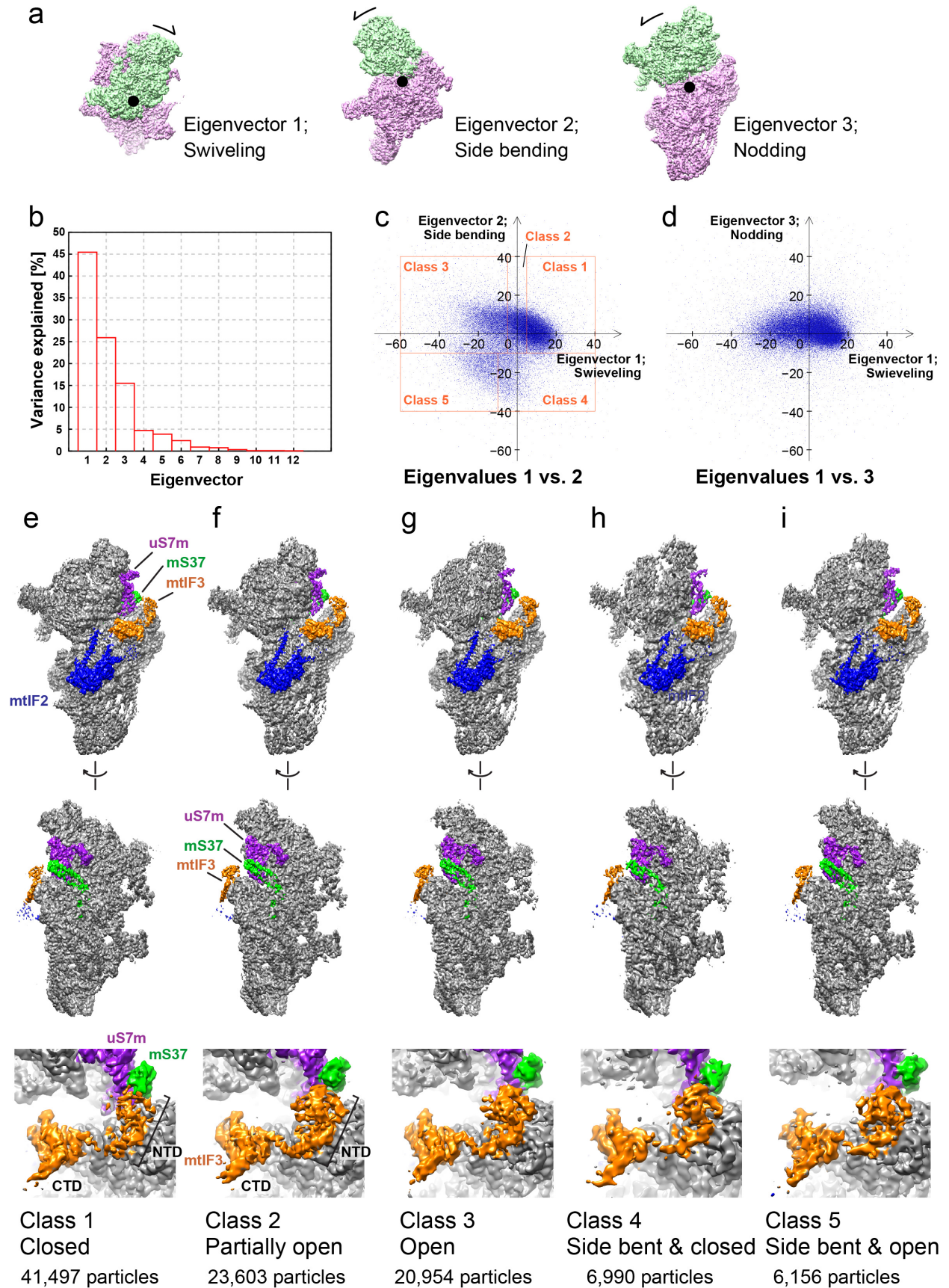
**a** Overview of the uS7m (violet) bound to the mtSSU head (yellow) located adjacent to the mtIF3 (orange). **b** Zoom-in panels illustrate the mtSSU head orientation for class 1 (closed) and class 3 (open) of the mtPIC-1. In class 1, two alternative conformations, non-shifted and shifted, are observed for the  $\beta$  hairpin of uS7m, which are colored purple and pink, respectively. The density map of the  $\beta$  hairpin is shown. In the closed conformation, mS37 is located in close vicinity of the mtIF3-NTD, whereas it moves away from the mtIF3-NTD in the open head conformation (class 3). **c** Superposition of the closed (shifted) and open state of the mtSSU head exhibits a movement of 10 Å of G165 in the  $\beta$  hairpin of uS7m. The h28 of 12S rRNA in closed (yellow) and open (green) states is highlighted. Positioning of U1468 of the h28 in both states is shown as spheres.



**Supplementary Figure 11. mS37 and mtIF3 coordinate movement of the mtSSU head.**

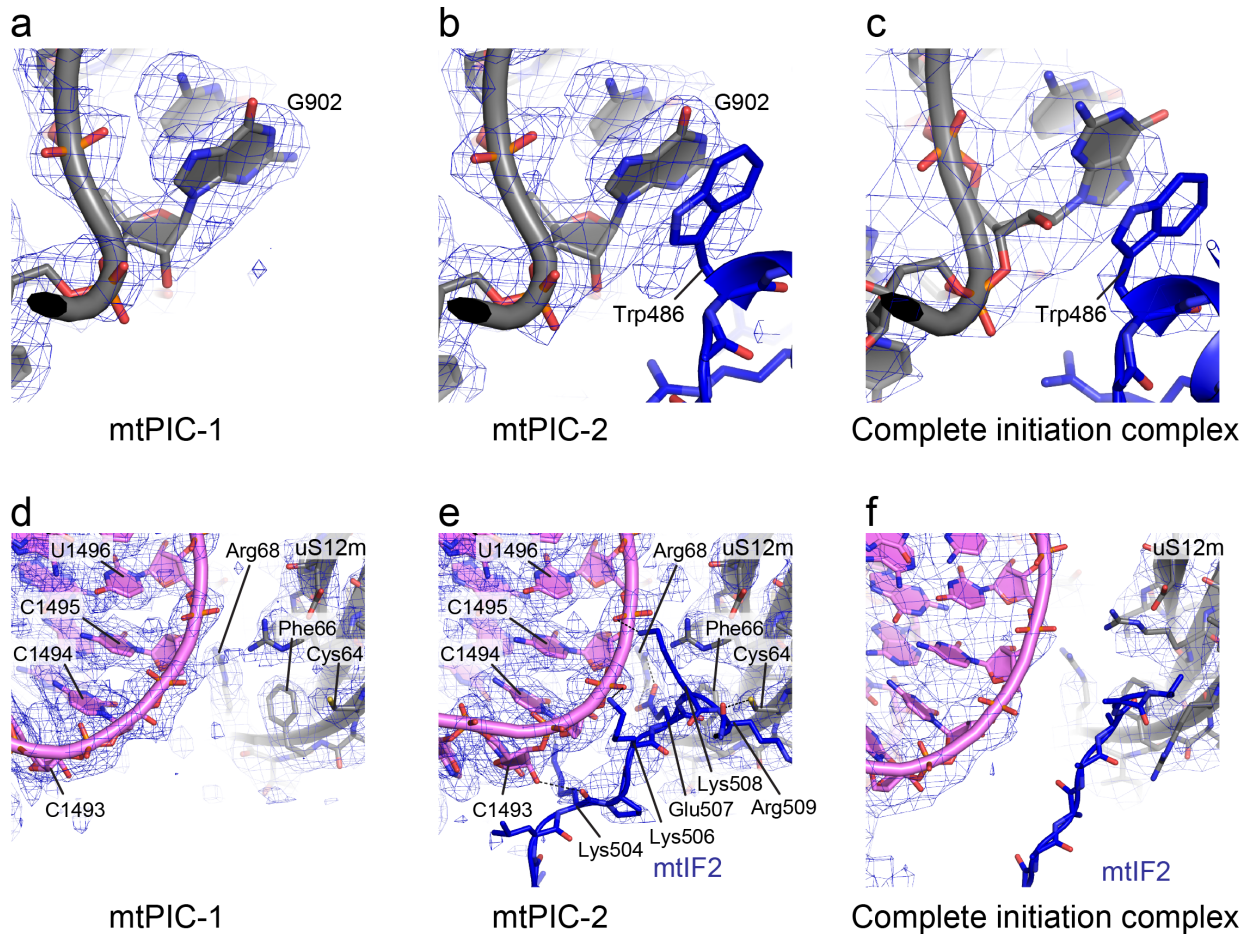
**a** The conformation of the mtSSU head is coordinated by the synergistic action of mS37 and mtIF3. mS37 lies in proximity to the mtIF3-NTD at the mtSSU platform, and cooperatively they restrict the rotation of mtSSU head towards more closed conformation that would clash with mtIF3 (the axis of rotation is shown by dotted line and gray arrow, the limitation of head movement is represented by red cross). **b** In bacterial system, the restricted SSU head movement and accommodation of IF2 is supported by IF3-IF1 interactions.





### **Supplementary Figure 12. Head motion analysis of mtPIC-2.**

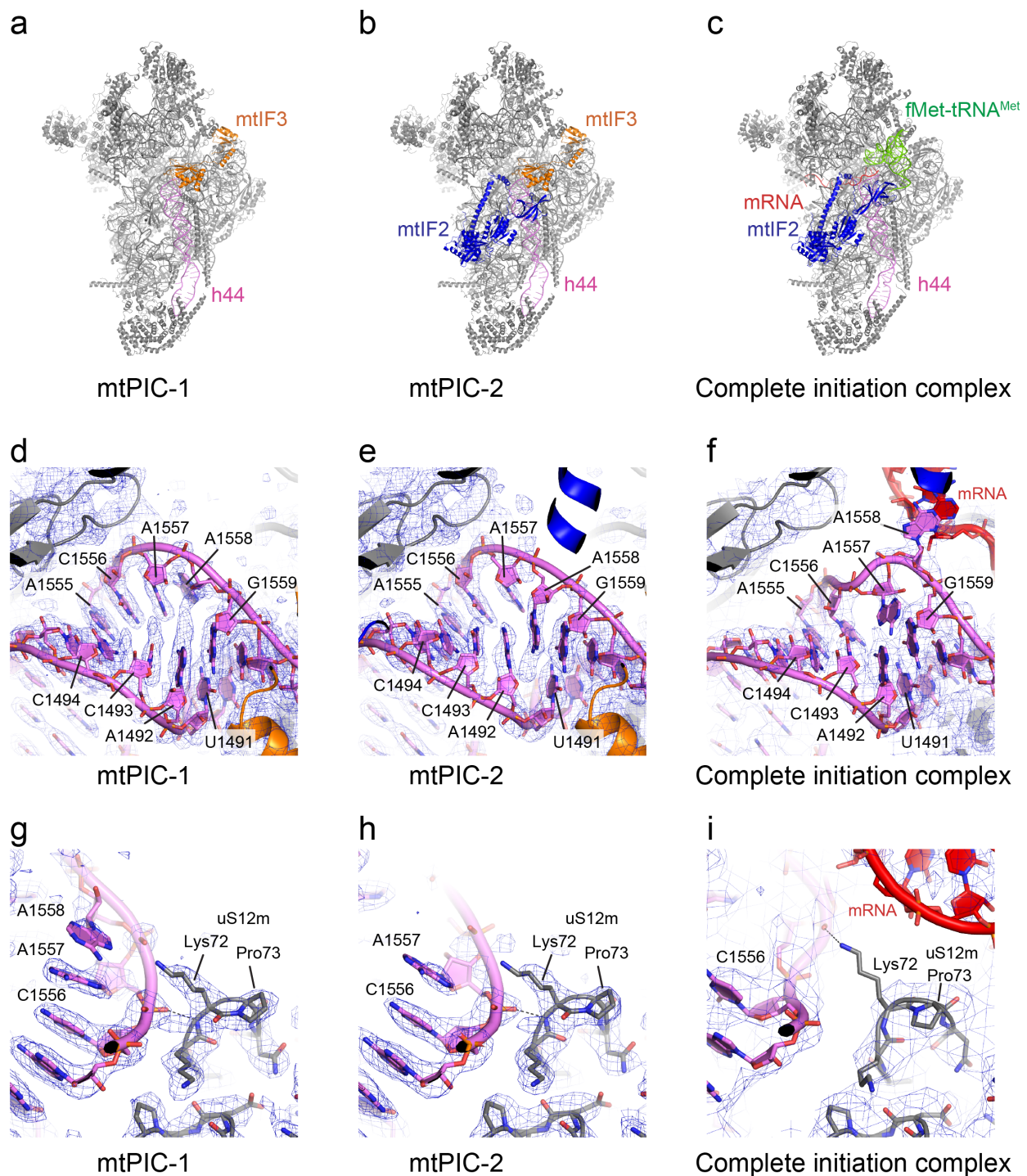
3D multibody analysis of the mtPIC-2 using the head and body masks (mtIF2 and mtIF3 are included in the body mask), similar in Fig. 3. Principal component analysis was done and the 1<sup>st</sup> to 3<sup>rd</sup> eigenvectors are mainly contributed by the head rotation, illustrated in **a**. The head and body are colored light green and pink, respectively. The rotation axis and the orientation are shown as a dot and an arrow, respectively. **b** Histogram of the variances explained by the 12 eigenvectors. **c**, **d** The eigenvalues (vectors 1, 2 and 3) of randomly chosen 100,000 particles are plotted two-dimensionally, against each other. Each particle is shown as a blue dot. The motions of the eigenvectors 1 (swiveling) and 2 (side bending) have non-gaussian distribution. Unlike in mtPIC-1, there are two peaks for the side bending motion. The particles are separated into five classes, based on the 1<sup>st</sup> and 2<sup>nd</sup> eigenvalues. Rectangle zones used for the classification are shown in **d**. **e-i** Classified particles are aligned to reconstitute their density maps. mtIF3, uS7m, and mS37 are colored orange, purple, and green, respectively. Similar to mtPIC-1, in the closed conformation, the density of the mtIF3-NTD is weaker and mS37 (green) and uS7m (purple) from the head contact to the mtIF3-NTD, suggesting the destabilization of the domain.



**Supplementary Figure 13. Comparison of the mtIF2 insertion domain and its interactions with the mtSSU between the mtPIC-2 and the complete initiation complex.**

**a-c** Zoomed-in views of G904 of 12S rRNA from mtPIC-1 (a) and mtPIC-2 (b), and the corresponding nucleotide from the complete initiation complex (c, PDB 6GAZ<sup>3</sup>). mtIF2 is colored blue. The cryo-EM densities are shown with the contour levels of 6.0, 6.0, and 7.0 (EMD-4369<sup>3</sup>), respectively. Trp486 from mtIF2 colored blue is stacking on G904, although the density is weak except for the indole ring. The densities support that G904 is in typical sugar and base conformations, i.e. C3'-endo and anti-conformations, respectively, in mtPIC-1 (a) and mtPIC-2 (b). In contrast, the corresponding nucleotide is modeled as C2'-endo and syn-conformations in the complete initiation complex (c).

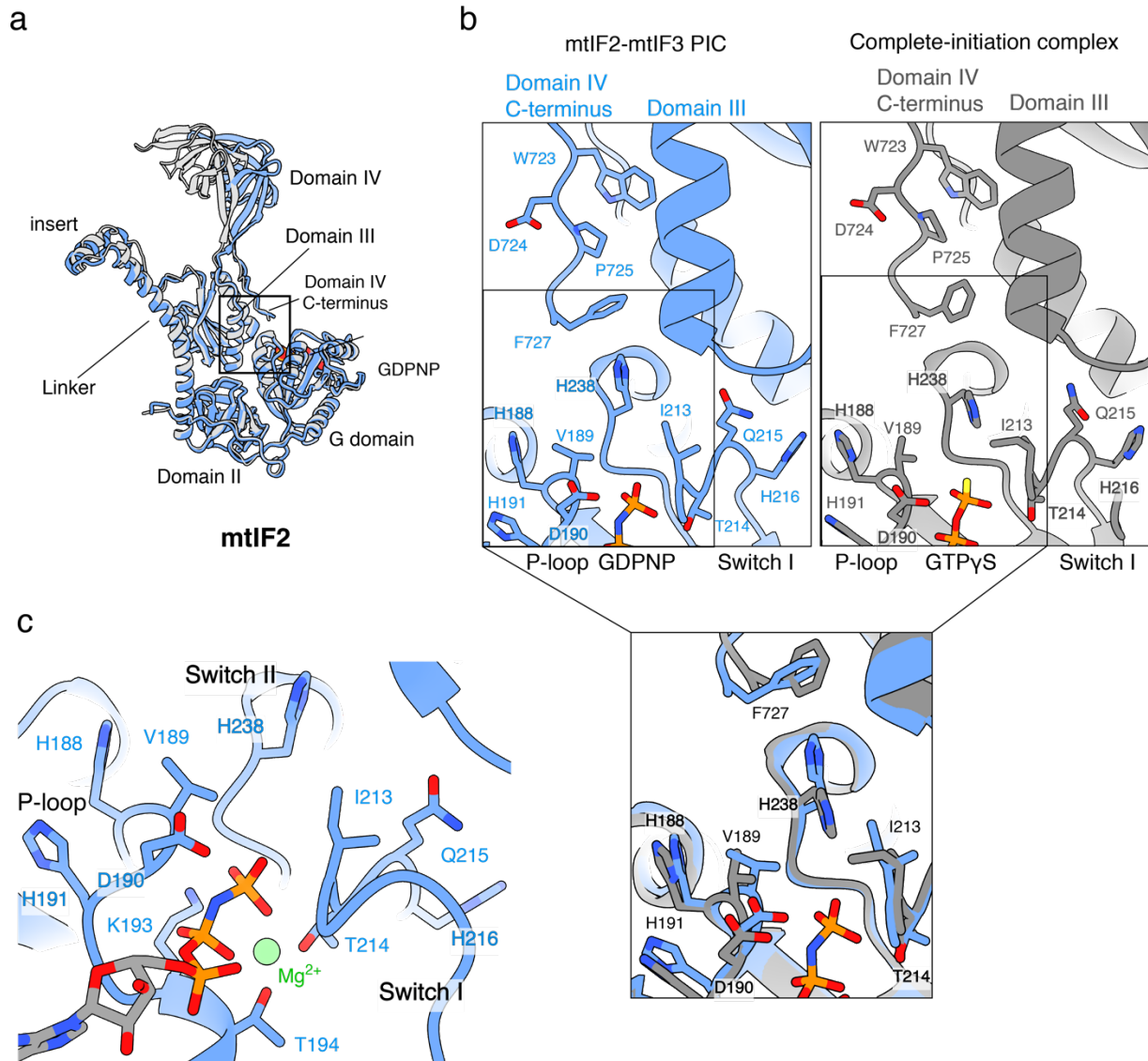
**d-f** The helix 44 and mtIF2 interactions. The helix 44 and mtIF2 are colored pink and blue, respectively. The cryo-EM densities are shown with the contour levels of 4.5, 4.5 and 5.0, respectively. In the mtIF2-mtIF3 bound complex, the density supports several interactions between mtIF2 and mtSSU through the helix 44 of 12S rRNA and uS11 (e). In the complete initiation complex, a poly alanine is placed in the mtIF2 region and no interaction from mtIF2 is observed (f), probably due to the conformational difference of the helix 44 of 12S rRNA.



**Supplementary Figure 14. Structure comparison of the helix 44 of 12S rRNA among the mtPICs and the complete initiation complex.**

**a-c** Overall structures of mtPIC-1 (**a**), mtPIC-2 (**b**), and the complete initiation complex (**c**, PDB 6GAZ<sup>3</sup>). The helix 44, mtIF2, mtIF3, mRNA, and fMet-tRNA<sup>Met</sup> are colored pink, orange, blue, red, and green, respectively. The helix 44 is surrounded by the factors. **d-f** Zoom-in views of the region 1492–1494 and 1557–1559 in the helix 44 from mtPIC-1 (**d**), mtI-2 (**e**), and the

corresponding region from the complete initiation complex (**f**). The cryo-EM densities are shown with the contour levels of 7.0, 7.0, and 6.0 (EMD-4369<sup>3</sup>), respectively. Although the density is a mixture of a few alternative conformations in mtPIC-1 and mtPIC-2, the majority is different. In mtPIC-1, there is a gap of base stacking between C1493 and C1494 (**d**) and A1558 is stacked on A1557. On the other hand, in mtPIC-2, A1492 and A1558 occupy the positions of C1493 and A1492 in mtPIC-1, respectively, which makes continuous base stacking from C1491:G1559 pair, A1558, A1492, C1493, to C1495:G1554 pair (**e**). The two universally conserved adenosines, A1557 and A1558, are known to flip out from the helix when the A-site tRNA comes. The first adenosine flips out and is stacking on a mRNA base in the complete initiation complex (**f**). The residues of the porcine mt-ribosome in the complete initiation complex are labeled according to the residue numbering in human. **g-i** Interaction between the helix 44 and uS12m. The cryo-EM densities are shown with the contour levels of 8.0, 8.0, and 3.0, respectively. In mtPIC-1 (**g**) and mtPIC-2 (**h**), Lys72-Pro73 in uS12m forms a cis peptide so that the main-chain NH group of Lys72 interacts to the phosphate group of A1557 of the helix 44. In contrast, the interaction is missing in the complete initiation complex (**i**) due to the conformational difference of the helix 44, and the Lys72-Pro73 forming a trans peptide.



### Supplementary Figure 15. mtIF2-dependent GTP hydrolysis.

**a** mtIF2 (blue) from the mtPIC-2 is superposed with mtIF2 (gray) from the complete initiation complex (PDB; 6GAW), shown independently of the mitoribosome. The C-terminus of domain IV and domain III lie in close proximity to the G-domain-bound GDPNP (boxed). **b** Zoom-in panels display the structures of the C-terminus of mtIF2 domain IV and the GTPase activation region from the mtPIC (blue) and the complete initiation complex (gray). Boxed areas from the above panels are superposed showing different conformational states for H238, V189, I213. **c** The mtIF2 G-domain bound-GDPNP shows several interactions with the P-loop, switch I and switch II. A magnesium ion (green, sphere representation) coordinates the  $\beta$  and  $\gamma$  phosphates of GDPNP. The conserved T214 (switch I) makes multiple interactions with the  $\gamma$  phosphate of GDPNP. The G4 (residues 288–291) and G5 (residues 324–326) motives interact with the guanosine moiety and the P-loop (residues 187–194) surrounds the phosphate groups of GDPNP.

**Supplementary Table 1. Cryo-EM data collection, processing, model refinement, and validation statistics.**

<b>Data collection</b>	mtPIC-1	mtPIC-2
Microscope	Titan Krios	Titan Krios
Detector	K2 Summit	K2 Summit
Magnification	165,000	165,000
Voltage [kV]	300	300
Total electron dose [ $e^-/\text{\AA}^2$ ]	30	30
Defocus range [ $\mu\text{m}$ ]	-0.25 to -5.0	-0.25 to -5.0
Pixel size [ $\text{\AA}$ ]	0.83	0.83
Final particles	379,761	103,165
Resolution [ $\text{\AA}$ ] (Overall/ masked body core/ head core/ tail/ mS39 region/ mtIF bound region)	2.97/ 2.87/ 2.85/ 3.11/ 3.04/ 2.85	3.14/ 3.04// 3.02/ 3.38/ 3.38/ 3.00
Map-sharpening $B$ factor [ $\text{\AA}^2$ ] (Overall/ masked body core/ head core/ tail/ mS39 region/ mtIF bound region)	-90/ -86/ -88/ -121/ -122/ -104	-84/ -83/ -89/ -122/ -116/ -73
<b>Model composition</b>		
Total atoms (non-hydrogen/ hydrogen)	68,869/ 59,430	73,335/ 63,948
Chains (RNA/ protein)	1/ 31	1/ 32
RNA residues (non-modified/ $m^5\text{U}$ / $m^4\text{C}$ / $m^5\text{C}$ / $m^6_2\text{A}$ )	949/ 1/ 1/ 1/ 1/ 2	949/ 1/ 1/ 1/ 1/ 2
Protein residues (non-modified/ $N$ -acetyl Ala)	5,918/ 2	6,489/ 2
Metal ions ( $\text{Mg}^{2+}$ / $\text{K}^+$ / $\text{Zn}^{2+}$ )	60/ 17/ 1	61/ 17/ 1
Ligands (GDPNP/ ATP/ $\text{NAD}^+$ / 2Fe-2S/ spermine/ streptomycin)	1/ 1/ 1/ 2/ 1/ 1	2/ 1/ 1/ 2/ 1/ 1
Waters	59	61
<b>Refinement</b>		
Model to map CC ( $\text{CC}_{\text{mask}}$ / $\text{CC}_{\text{box}}$ / $\text{CC}_{\text{peaks}}$ / $\text{CC}_{\text{volume}}$ )	0.84/ 0.85/ 0.80/ 0.84	0.85/ 0.86/ 0.80/ 0.85
Average $B$ factor [ $\text{\AA}^2$ ] (Overall/ RNA/ protein/ metal ion and ligand/ water)	36.4/ 35.2/ 36.8/ 31.1/ 25.5	42.4/ 29.4/ 46.3/ 33.7/ 19.2
RMSD bond lengths [ $\text{\AA}$ ]	0.005	0.005
RMSD bond angles [ $^\circ$ ]	0.67	0.66
<b>Validation by MolProbity</b>		
Clash score	2.1	2.2
Rotamer outliers [%]	0.06	0.05

Ramachandran plot [%] (Favored/ allowed/ disallowed)	96.97/ 2.97/ 0.05	96.95/ 3.01/ 0.05
<b>EMDB ID</b> (Overall/ masked body core/ head core/ tail/ mS39 region/ mtIF bound region)	10021/ 10023/ 10024/ 10025/ 10026/ 10027	10022/ 10028/ 10029/ 10030/ 10031/ 10032/
<b>PDB ID</b>	6RW4	6RW5



**Supplementary Table 2. Modeled RNA and proteins of the mtPIC.**

Name	Uniprot ID	Chain ID	Modeled residues	Predicted mature RNA/protein	Notes
12S rRNA	NR_137294.1 (Ref_seq) NC_012920.1 (Ref_seq mt-gDNA)	A	648–1602	648–1601	A750G and A1438G variant. Known modifications: m <sup>5</sup> U1076, m <sup>4</sup> C1486, m <sup>5</sup> C1488, m <sup>6</sup> <sub>2</sub> A1583, m <sup>6</sup> <sub>2</sub> A1584. NAD <sup>+</sup> interacting U948 and A1046. Spermine interacting U944, G945, U946, U1044, G1045, C1048. Streptomycin interacting G899, A1167, A1555, C1556.
bS1m	Q9Y2Q9	W	76–175	72–187	
uS2m	Q9Y399	B	53–277	1–296	Asp224, Asp240, Asp241 and His93 seem to coordinate an Mg <sup>2+</sup> or K <sup>+</sup> ion instead of a Zn <sup>2+</sup> .
uS3m	Q96EL2	C	36–167	36–167	
uS5m	P82675	D	88–430	1–430	
bS6m	P82932	E	2–123	1–125	Cys105 participates in a 2Fe-2S cluster coordination with bS18m.
uS7m	Q9Y2R9	F	35–242	38–242	
uS9m	P82933	G	50–176, 194–396	1–396	His51 seems interacting to an Mg <sup>2+</sup> ion coordinated by 12S rRNA in the SSU body.
uS10m	P82664	H	50–189	1–201	
uS11m	P82912	I	58–194	1–194	
uS12m	O15235	J	31–138	30–138	Cis peptide at Pro73.
uS14m	O60783	K	28–128	1–128	
uS15m	P82914	L	63–236	58–257	
bS16m	Q9Y3D3	M	10–128	35–137	Cys26 participates in a 2Fe-2S cluster coordination with mS25.
uS17m	Q9Y2R5	N	4–113	21–130	
bS18m (bS18c)	Q9Y3D5	P	46–142	1–142	Cys65, Cys68 and Cys100 coordinate a 2Fe-2S cluster with bS6m Cys105.
bS21m	P82921	Q	2–87	1–87	N-acetylated Ala2. Cys50Arg variant.
mS22	P82650	R	64–358	1–360	
mS23	Q9Y3D9	S	2–136	2–190	
mS25	P82663	T	2–169	1–173	Cys139, Cys141 and Cys149 coordinate a 2Fe-2S cluster with bS16m Cys26.
mS26	Q9BYN8	U	27–202	28–205	
mS27	Q92552	V	29–293, 311–407	37–414	
mS29	P51398	X	47–398	22–398	GDP in the previous reports seems to be ATP with an Mg <sup>2+</sup> ion. Another nucleotide binds next to Tyr173, which is GTP or GDPNP. Cis peptide at Pro339.
mS31	Q92665	Y	247–395	66–395	Cis peptide at Pro314.
mS33	Q9Y291	Z	3–102	2–106	
mS34	P82930	0	4–218	1–218	
mS35	P82673	1	48–323	?–323	
mS37	Q96BP2	2	2–118	1–118	N-acetylated Ala2. Possible disulfide bonds of Cys45-Cys76 and Cys55-Cys66.
mS38	Q9NWT8	3	128–197	1–199	

mS39	Q96EY7	4	55–207, 232–666	38–689	Cis peptides at Pro135 and Pro483.
mS40 (bS18b)	Q9Y676	0	46–239	36–258	Zn <sup>2+</sup> coordination (Cys94, Cys105, Cys108, Cys143).
mtIF2	P46199	7	157–727	30–727	GDPNP with an Mg <sup>2+</sup> ion bound.
mtIF3	Q9H2K0	8	72–262	32–278	The68Ile, Phe243Leu variant.

**Supplementary Table 3. Comparison of polar and stacking interactions between mtIF3 and mtSSU in this study and Koripella *et al.* <sup>6</sup>.**

mtIF3	Region	mtSSU	Type	Koripella et al.
Ser76 side chain	NTD	rRNA G988 phosphate	H bond	Not observed
Asn77 side chain	NTD	uS11m Thr114 main chain	H bond	Not observed
Asn77 main chain	NTD	uS11m Arg118 side chain	H bond	Not observed
Asp113 side chain	NTD	uS11m Arg138 side chain	H bond/ionic	Not observed
Arg115 side chain	NTD	rRNA A987 phosphate	H bond/ionic	Not observed
Arg115 side chain	NTD	uS11m Thr114 main chain	H bond	Observed
Gly133 main chain	Linker	rRNA A987 ribose	H bond	Not observed
Leu137 side chain	Linker	rRNA A987 base	Stacking	Observed
Arg140 side chain	Linker	rRNA A987 base	H bond	Not observed
Arg140 side chain	Linker	rRNA A987 ribose	H bond	Observed
Arg140 side chain	Linker	rRNA G988 base	Stacking	Observed
Arg140 side chain	Linker	rRNA U1000 base	H bond	Not observed
Arg144 side chain	Linker	rRNA C999 phosphate	H bond/ionic	Observed
Arg144 side chain	Linker	rRNA U1000 phosphate	H bond/ionic	Observed
Lys159 side chain	CTD	rRNA U1077 base	H bond	Not observed
Lys159 side chain	CTD	rRNA A1080 phosphate	H bond/ionic	Not observed
Glu160 main chain	CTD	rRNA A1078 ribose	H bond	Observed
Glu160 main chain	CTD	rRNA A1079 phosphate	H bond	Not observed
Ser164 side chain	CTD	rRNA C1561 phosphate	H bond	Not observed
Asn166 side chain	CTD	rRNA U1560 phosphate	H bond	Not observed
Gly168 main chain	CTD	rRNA U1560 ribose	H bond	Observed
His170 side chain	CTD	rRNA U1490 ribose	H bond	Not observed
Asp171 side chain	CTD	rRNA U1560 ribose	H bond	Observed
Lys175 side chain	CTD	rRNA G1562 phosphate	H bond/ionic	Observed
Gln178 side chain	CTD	rRNA G1079 ribose	H bond	Observed but differently

Trp182 side chain	CTD	rRNA A1080 phosphate	H bond	Not observed
-------------------	-----	----------------------	--------	--------------

All the listed interactions are supported by the cryo-EM density of mtPIC-1.

Simple Van der Waals (VDW) interactions are not listed.

All the interactions described in Koripella et al. <sup>6</sup> are observed, except for those through mtIF3 Phe75, Val78, Arg80 and Lys81. Phe75 is away from mtSSU in our model. Val78 is away from rRNA, rather than in VDW distance from Gly116 of uS11m. Arg80 side chain does not point to mtSSU, rather than making an internal salt bridging with Asp110. Lys81 in our model seems to point to uS7m in the head of mtSSU, instead to uS11m.

The differences seem to be due to the resolution improvement.

**Supplementary Table 4. *In vitro* translation initiation assay using fluorescently labeled components: Cy5-mtIF3, Cy3-fMet-tRNA<sup>Met</sup>, and Atto390-mRNA.**

	1	2	3	4	5	6
	mtSSU+ mtIF2 + mtIF3	mtSSU + mtIF2 + tRNA	mtSSU+ mtIF2 + mtIF3 + mRNA	mtSSU+ mtIF2 + tRNA + mRNA	mtSSU + mtIF2 + mtIF3 + tRNA	mtSSU+ mtIF2 + mtIF3 + tRNA + mRNA
<b>mtIF3- Cy5</b>	58±7%	N/A	55±8%	N/A	34±5%	41±7%
<b>fMet- tRNA- Cy3</b>	N/A	23±6%	N/A	26±2%	22±3%	20±4%
<b>mRNA- Atto390</b>	N/A	N/A	0	0	N/A	0

Translation initiation reactions were performed as described in methods, using the fluorescently labeled components presented in the Table. After purification of the initiation complex, the concentration of each labeled species was measured and normalized to the mtSSU concentration. We did not detect fluorescence of the Atto390-labeled mRNA in any of the described conditions, indicating that the mRNA is not loaded on the mtSSU, but only after binding of the mtLSU. The data presented in the Table were complemented with the fluorescence cross-correlation spectroscopy analysis (Fig. 3b and Supplementary Fig. 9), to investigate if mtIF3 and tRNA bind to the same mtSSU. Data are derived from the mean values (n=3). Error bars represent the standard deviation. Source data are provided as a Source Data file.

**Supplementary Table 5. Polar and stacking interactions between mtIF2 and mtSSU in the mtPIC-2 and the complete initiation complex.**

mtIF2	Region	mtSSU	Type	Kummer et al. <sup>3</sup>
Lys366 main chain	Linker	rRNA U821 ribose	H bond	Observed
Gly367 main chain	Linker	rRNA A695 base	Stacking	Observed
Lys383 main chain	Linker	rRNA U832 phosphate	H bond/ionic	Not observed
Arg397 side chain	Linker	rRNA U821 phosphate	H bond/ionic	Observed
Arg397 side chain	Linker	rRNA U831 phosphate	H bond/ionic	Observed
Asp459 side chain	Linker	uS12m Thr101 side chain	H bond	Observed
Lys466 side chain	Insertion	uS12m His100 main chain	H bond	Not observed
Arg467 main chain	Insertion	rRNA A892 ribose	H bond	Observed
His470 side chain	Insertion	rRNA C891 ribose	H bond	Observed
His474 side chain	Insertion	rRNA C890 phosphate	H bond	Observed
Gln475 side chain	Insertion	rRNA G889 phosphate	H bond	Observed
Arg478 side chain	Insertion	rRNA G889 ribose	H bond/ionic	Observed
Arg478 side chain	Insertion	rRNA C890 phosphate	Ionic	Observed
Trp486 side chain	Insertion	rRNA G902 base	Stacking	Observed
Lys504 main chain	Linker	rRNA C1493 ribose	H bond	Not observed
Lys504 side chain	Linker	rRNA C1494 base	H bond	Not observed
Lys506 side chain	Linker	rRNA C1495 phosphate	H bond/ionic	Not observed
Glu507 side chain	Linker	uS12m Phe66 side chain	Stacking	Not observed
Glu507 side chain	Linker	uS12m Arg68 side chain	H bond/ionic	Not observed
Lys508 side chain	Linker	rRNA U1496 phosphate	H bond/ionic	Not observed
Arg509 main chain	Linker	uS12m Cys64 side chain	H bond	Not observed

All the listed interactions are supported by the cryo-EM density of mtPIC-2.

Simple VDW interactions are not listed.

All the interactions described in Kummer et al. <sup>3</sup> are observed, except for those through mtIF2 Lys487, Arg489, Ser490, and Phe949.

The interactions through the loop consists of the residue 479–513 in mtIF2 are different due to the conformational difference of h44 of rRNA.

**Editorial Note:** This manuscript has been previously reviewed at another journal that is not operating a transparent peer review scheme. This document only contains reviewer comments and rebuttal letters for versions considered at Nature Communications.

REVIEWERS' COMMENTS:

Reviewer #1 (Remarks to the Author):

In my original review, I had concerns that mtIF3 might move on the mtSSU to accommodate tRNA. The additional structural analysis provided in the revised manuscript has allayed my concerns.

My other major concern was that insufficient evidence was provided in the original manuscript to support the model that mRNA binds to the monosome but not the SSU. Here, the authors provide further support for their "monosome only" model through the use of single-molecule imaging (optical tweezers combined with confocal fluorescence microscopy). These experiments are a great addition to the paper.

In light of the improvements to the manuscript, I recommend that the paper is published. The findings are novel and the structural biology is done to a very high standard.

Reviewer #2 (Remarks to the Author):

The initiation of mitochondrial translation is a process of fundamental importance, which is still poorly characterized. Here Khawaja et al. have studied the initiation of translation in mitochondria. A biochemical reconstitution included a mitochondrial small subunit (mtSSU) bound to mtIF3 to which recombinant mtIF2-GMPPNP and initiator tRNA were added. Samples of this reaction mixture were subsequently analyzed by cryo-EM to reveal two distinct states. The first state contains mtSSU-mtIF3 whereas the second contains mtSSU-mtIF2-mtIF3. The structural biology analysis that is presented in this manuscript is of exceptional quality and the interpretation of the structural data is outstanding.

Subsequent biochemical studies (using fluorescence cross-correlation spectroscopy and single-molecule imaging) were used to obtain further insights into the mechanism of mitochondrial translation initiation where the authors found that monosomes but not mtSSU complexes are associated with messenger RNAs. The authors conclude that there are key differences between bacterial and mitochondrial translation initiation so that during mitochondrial translation initiation mRNA only associates with monosomes and not mtSSU complexes.

The authors have revised several key points after their initial submission, and I believe that this manuscript is of clear interest to the readership of Nature Communications and should therefore be published provided that the following point is addressed:

The available biochemical data can be explained by two different models for mitochondrial translation initiation (1. mRNA associates late (with monosomes; c.f. Figure 5) or 2. mRNA associates very weakly with mtSSU complexes earlier) while the authors have only illustrated the first model in Figure 5.

The existing biochemical data shows that:

1. Monosomes are the only species that is found to be stably associated with mRNAs when using FCCS (Fig.2).
2. Monosomes are the only species that stably bind to mRNA in single-molecule experiments (Fig. 5).

The existing biochemical data however does not rule out that:

1. mtSSU-mRNA complexes are very transient and cannot be detected with the employed techniques.

In the absence of Shine-Dalgarno and anti-Shine-Dalgarno sequences it is expected that mtSSU-mRNA interactions are weaker than in bacteria. The addition of the mtLSU would be expected to enhance mRNA affinity so that monosomes should have a higher affinity for mRNAs than mtSSUs. This is consistent with the data shown in Figures 2 and 5.

Based on the above points, it is equally possible (but only stated by the authors in the last two sentences of the manuscript) that mitochondrial translation initiation could involve mRNA joining at an earlier point via transient intermediates.

To address this point clearly, the easiest way would be to change the model proposed in Figure 5 so that mRNA joins at the same time as mtLSU and initiator tRNA because the current temporal resolution does not allow us to distinguish between these options. Importantly, this model would:

- a. Capture all available data as this point is still not fully addressed.
- b. Include a model in which mRNA may bind after mtLSU or before mtLSU binding.
- c. Leave enough room for further in-depth mechanistic analyses, which are beyond the scope of this manuscript, to be performed in the future.

Reviewer #3 (Remarks to the Author):

I had the pleasure of reviewing this manuscript in its previous incarnation. I was thoroughly impressed and found it compelling, as it reports a translation initiation pathway that is unique to mitochondria, albeit that it may occasionally occur in bacteria. The authors have now performed some very delicate molecular tweezers expts to address comments from a reviewer who has suggested that weak interaction of various components in the pre-initiation pathway may have been lost during sucrose gradient centrifugation. This new data fully supports the authors pathway. I very much like this work and strongly support its publication. In the Life Sciences, nothing is ever fully black and white. Of course, there are some highly unlikely scenarios that may occur that could argue against the data presented to support this pathway, but I think the authors have done more than enough to lead to publication of what is quite a provocative and exciting novelty that once again supports the idea that mitochondria do things their own way!



We thank the referees for their constructive inputs that helped us to improve the manuscript, and are happy that they are satisfied with our revision. The only outstanding point was raised by referee 2, and we fully addressed it as requested by changing the proposed Figure 5 so that mRNA joins at the same time as mtLSU. More detailed response is described below:

Referee 2:

“The existing biochemical data however does not rule out that:

1. mtSSU-mRNA complexes are very transient and cannot be detected with the employed techniques.

In the absence of Shine-Dalgarno and anti-Shine-Dalgarno sequences it is expected that mtSSU-mRNA interactions are weaker than in bacteria. The addition of the mtLSU would be expected to enhance mRNA affinity so that monosomes should have a higher affinity for mRNAs than mtSSUs. This is consistent with the data shown in Figures 2 and 5.

Based on the above points, it is equally possible (but only stated by the authors in the last two sentences of the manuscript) that mitochondrial translation initiation could involve mRNA joining at an earlier point via transient intermediates.

To address this point clearly, the easiest way would be to change the model proposed in Figure 5 so that mRNA joins at the same time as mtLSU and initiator tRNA because the current temporal resolution does not allow us to distinguish between these options. Importantly, this model would:

- a. Capture all available data as this point is still not fully addressed.
- b. Include a model in which mRNA may bind after mtLSU or before mtLSU binding.
- c. Leave enough room for further in-depth mechanistic analyses, which are beyond the scope of this manuscript, to be performed in the future.”

We agree with the referee that with our current experimental setup we are not able to discriminate whether mRNA binds before or after mtLSU joining.

We have now modified the model in Figure 7 (previously Figure 5) to accommodate both possibilities. We also highlighted it in the figure legend:

‘Joining of the mtLSU may result in the conformational change of mtIF2 and GTPase activation that leads to tRNA and mRNA accommodation. Alternatively, transient binding of mRNA and tRNA (not detected with our techniques) to the mtSSU after mtIF3 departure precede recruitment of the mtLSU.’

Finally, in the abstract ‘reveal’ was replaced with ‘suggest’ in order not to rule out other possible states.